Understanding non-ideal paleointensity recording in igneous rocks: Insights from aging experiments on lava samples and the causes and consequences of 'fragile' curvature in Arai plots

L. Tauxe[1*], C.N. Santos[1], B. Cych[1], X. Zhao[2], A.P. Roberts[2], L. Nagy[1], and W. Williams[3]

[1]Scripps Institution of Oceanography, University of California, San Diego, La Jolla, CA, USA
[2]Research School of Earth Sciences, Australian National University, Canberra, Australia
[3]School of Geosciences, University of Edinburgh, James Hutton Road, Edinburgh, EH9 3FE, UK

Key Points:

- Unequal blocking/unblocking temperature spectra can lead to biased paleointensity estimates.
- Inequality grows through time in samples with coarser magnetic grain sizes.
- Quantifying curvature in Arai plots and the use of iFORCs can identify possibly biased results.

*National Science Foundation

Corresponding author: Lisa Tauxe, ltauxe@ucsd.edu

Abstract

The theory for recording of thermally blocked remanences predicts a quasi-linear relationship between low fields like the Earth's in which rocks cool and acquire a magnetization. This serves as the foundation for estimating ancient magnetic field strengths. Addressing long-standing questions concerning Earth's magnetic field require a global paleointensity dataset, but recovering the ancient field strength is complicated because the theory only pertains to uniformly magnetized particles. A key requirement of a paleointensity experiment is that a magnetization blocked at a given temperature should be unblocked by zero-field reheating to the same temperature. However, failure of this requirement occurs frequently and the causes and consequences of failure are incompletely understood. Recent experiments demonstrate that the remanence in many samples typical of those used in paleointensity experiments is unstable, exhibiting an "aging" effect in which the (un)blocking temperature spectra can change over only a few years resulting in non-ideal experimental behavior. While a fresh remanence may conform to the requirement of equality of blocking and unblocking temperatures, aged remanences may not. Blocking temperature spectra can be unstable (fragile), which precludes reproduction of the conditions under which the original magnetization was acquired. This limits our ability to acquire accurate and precise ancient magnetic field strength estimates because differences between known and estimated fields can be significant for individual specimens, with a low field bias. Fragility of unblocking temperature spectra may be related to grain sizes with lower energy barriers and may be detected by features observed in first-order reversal curves.

Plain Language Summary

Earth's magnetic field acts as a shield against energetic solar storms and is thought to have been important in the evolution of life on Earth. The magnetic field is currently dropping rapidly in strength. Answering questions like 'What is the average field?' and 'What is the likelihood of a collapse associated with a reversal or excursion?' depends on our understanding of past field behavior. There are no human measurements of field strength prior to the 19^{th} century, so we rely on igneous and archaeological records. A great deal of effort has been put into experimental protocols to develop reliable records of field strength and to assess data reliability. Yet, mysteries remain regarding the nature of these records. This paper focuses on expanding our understanding of magnetic recording in lava samples, which are one of the main archives used in paleointensity studies. In particular, we investigate the causes and consequences of failure of the principal assumptions in paleointensity experiments which appears to result in biased estimates.

1 Introduction

The strength of the geomagnetic field has been a focus of geophysical research since the 1930s, starting with the work of Königsberger (1936) and Thellier (1938) and continuing today (see review of Tauxe and Yamazaki (2015)). Absolute paleointensity experiments rely on the assumption from Néel theory (Néel, 1949) that thermal remanent magnetizations (TRMs) are related quasi-linearly to the field in which a sample cooled and are generally based on normalization of remanences in controlled laboratory fields.

Despite decades of effort, fundamental problems remain with the methods used to extract reliable records of field strength. Paleointensity experiments involve a variety of protocols and there is no consensus on what materials might be suitable for the experiment or what constitutes a 'reliable' result. Although the paleointensity community recognized early the value of testing methods on materials with TRMs acquired in known fields (Abokodair, 1977; Tanaka & Kono, 1991), recent compilations suggest that even a single lava flow can give widely divergent results with different methods yielding sig-

nificantly different results (Cromwell et al., 2015; Tauxe et al., 2016; Cai et al., 2017; Cromwell et al., 2018).

1.1 Thellier's Laws and paleointensity experimental design

Most paleointensity data in global paleomagnetic databases, e.g., the MagIC database (Tauxe et al., 2016) or the PINT database (Biggin, 2010), were obtained through some variant of the classic Königsberger-Thellier-Thellier (KTT) double heating technique (Koenigsberger, 1938; Thellier & Thellier, 1959) where the initial remanence (assumed to be a TRM) is replaced in a step-wise fashion with a laboratory-acquired partial TRM (pTRM), the remanence acquired by cooling through two temperatures T_1, T_2 below the Curie Temperature.

The basic theoretical underpinnings of KTT experiments are the so-called 'Thellier laws' (Thellier, 1938; Thellier & Thellier, 1959) that concern pTRMs. The Law of Independence states that pTRMs blocked between two temperature steps are independent of pTRMs acquired at different blocking temperatures, and the Law of Additivity requires that the total TRM (TTRM) is the sum of all pTRMs. But the most important of these is the Law of Reciprocity, where the blocking temperature (T_b) at which a pTRM was acquired is the same at which it is destroyed (the unblocking temperature, T_{ub}) and it is this law that is the focus of this paper.

Despite widespread use, KTT techniques have drawbacks in practice. These include complications such as changing of the ability to acquire a pTRM through chemical alteration during the double heating experiments (Coe, 1967), non-linearity of the TRM with applied field (Selkin et al., 2007), the effect of the rate at which the recording medium cooled (S. Halgedahl et al., 1980; Dodson & McClelland-Brown, 1980), and anisotropy of the remanence tensor (Aitken et al., 1981). These phenomena can in many cases be detected, and in the latter three cases adjusted for. However, there are more difficult complications with less well understood causes and consequences. For example, there is increasing evidence that paleointensity estimates from materials with non-linear Arai plots are biased (Krása et al., 2003; Shaar & Tauxe, 2015; Cromwell et al., 2015; Smirnov et al., 2017; Cromwell et al., 2018). However, the causes of bias are poorly understood and appropriate remedies are presently unavailable. We suspect that the most likely cause of bias is failure of the Law of Reciprocity.

The Law of Reciprocity requires that a pTRM acquired (blocked) by cooling through a particular temperature, T_b, can be removed (unblocked) by heating to the same temperature (T_{ub}) and cooling in zero field. Many experimental protocols specify the order in which steps are performed in order to detect failure of one or more of Thellier's Laws. The protocol we use here is the so-called IZZI protocol (Yu et al., 2004; Tauxe & Staudigel, 2004), which is designed specifically to include a test of the Law of Reciprocity. In this approach, specimens are heated to a given temperature and then cooled either in the presence of a controlled laboratory field (an in-field step) or in zero field (a zero-field step). The order (in-field followed by a zero-field step, IZ) alternates with a zero-field step first followed by an in-field step (ZI).

As a conceptual model to illustrate the role of similar or different blocking and unblocking temperature spectra, we use a phenomenological approach similar to that taken by Paterson et al. (2015) (see also Fabian (2001); Yu et al. (2004), and Biggin (2006)). We draw synthetic (un)blocking temperature spectra from a scaled beta distribution with shape parameters (α and β). When Thellier's Laws are obeyed, particularly the Law of Reciprocity, blocking and unblocking temperature spectra are identical (Figure 1a). When subjected to an IZZI-modified KTT type experiment, the initial TRM is replaced by pTRMs in a step-wise fashion (Figure 1b). In the ideal case, there is a linear relationship between the TRM remaining after heating to a given temperature step and the pTRM gained as shown in the Arai plot in Figure 1c.

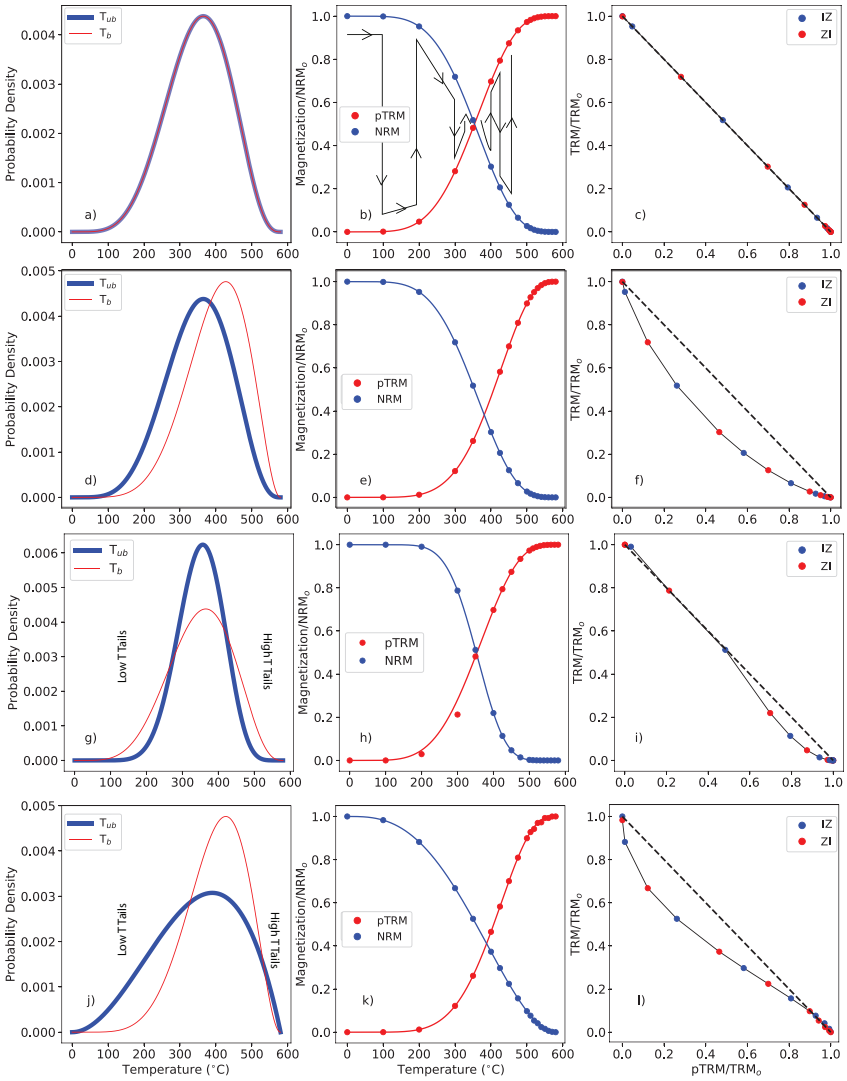

Figure 1. Phenomenological model of the effect of unequal pTRM blocking and unblocking in Arai plots. Left-hand panels: distribution of (un)blocking temperatures. Blue and red are the unblocking and blocking temperature (T_{ub}, T_b) spectra, respectively. Middle panels: NRM demagnetization (blue) and pTRM acquisition (red). The order in which the steps are taken alternates between NRM demagnetization (zero-field cooling) first and pTRM acquisition (in-field cooling) first as shown in b). Right-hand panels: plots of TRM remaining versus pTRM gained. Data for in-field followed by zero-field (IZ) steps first are indicated as blue dots; zero-field followed by in-field cooling (ZI) steps first are indicated as red dots. Heavy dashed lines are the relationship predicted by Néel theory. a-c) A case in which blocking and unblocking temperature spectra are identical (Law of Reciprocity obeyed). d-f) A case in which the unblocking temperature spectrum is shifted to lower temperatures than the blocking temperatures. g-i) A case in which the blocking temperature spectrum is wider than the unblocking temperature spectrum with both high and low temperature tails. j-l) A case in which the unblocking temperature spectrum is broader than the blocking temperature spectrum.

Thellier's laws are only strictly true for non-interacting uniaxial single domain (SD) magnetic particles whose behavior is understood using the theory of Néel (1949, 1955). In Figure 1d-f, we show an example of a case in which the unblocking temperature spectrum (blue) is somewhat lower than the blocking temperature spectrum (red). The resulting Arai plot sags below the theoretical line (heavy dashed line Figure 1f).

When the unblocking temperature spectrum is narrower than the blocking temperature spectrum (Figure 1g), the Arai plot is 'hook' shaped (Figure 1i) and when there is a large low temperature bias to the unblocking temperature spectrum with a small high temperature component, the Arai plot is 'S'-shaped (Figure 1l). The ultimate cause of sagging, 'hook', or S-shaped Arai plots stems from a failure to satisfy the Law of Reciprocity where remanence can be removed at either a lower temperature than originally imparted (low-temperature pTRM tails) or at a higher temperature (high-temperature pTRM tails), respectively. In this paper, we focus on possible causes and consequences of the widely observed 'sagging' in Arai plots (including the hooked and S-shaped curves in Figure 1i and l, respectively), while ignoring the influence of chemical alteration, nonlinearity in TRM response, cooling rate or anisotropy effects.

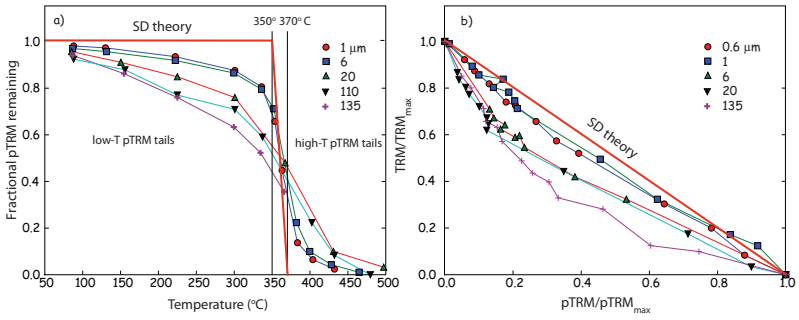

Figure 2. a) Stepwise thermal demagnetization of pTRMs imparted by applying a small DC field during cooling from 370 to 350°C in magnetite of known grain size. Between 50 and 90% of the remanence unblocks below (a low temperature pTRM tail) or above (a high temperature pTRM tail) the pTRM blocking temperature range. Failure of reciprocity is most extreme for the largest grain sizes. b) Arai plots for paleointensity experiments on the synthetic specimens shown in a). Note that the x-axis is somewhat unusual in that the pTRM was normalized by the maximum pTRM acquired (total TRM) and not the initial TRM as is the usual practice. [Data of Dunlop and Özdemir (2001); figure modified from Tauxe et al. (2010).]

1.2 Sagging Arai plots in synthetic samples

Dunlop and Özdemir (2001) reported results from a suite of specimens whose grain sizes were well known and likely to be multi-domain (MD). They imparted a pTRM over a narrow temperature interval (370 to 350°C), and thermally demagnetized them to 500°C in a step-wise fashion. The remanence remaining at each temperature step is shown in Figure 2a. The heavy red line is the prediction from theory for SD particles. Clearly the Law of Reciprocity is violated by all specimens, and the larger the grain size, the larger the deviation from theory. The portion of pTRM lost by heating to below the blocking temperature is termed a 'low-temperature pTRM tail' and that above is a 'high temperature pTRM tail'.

As predicted by the phenomenological models like those shown in Figure 1, the tails have a profound effect on the outcome of double heating experiments as shown in Fig-

ure 2b. An Arai plot for the largest particles (135 μm) which are dominated by low temperature tails, sag below the ideal line, similar to the simulated Arai plot in Figure 1f. For smaller particle sizes (e.g., 1 μm) with larger high temperature tails, the curve is S-shaped, similar to those shown in Figure 1l.

If a particle is large enough to be non-uniformly magnetized, e.g., in the flower or vortex magnetic states (Williams & Dunlop, 1989; Schabes & Bertram, 1988), or the MD state, its magnetic behavior cannot be described by the analytical theory of Néel (1949). Just below the Curie temperature, magnetic particles are close to saturation, but as particles cool, more complex domain structures can form. In the case presented by Dunlop and Özdemir (2001), the particles were almost certainly MD and the failure of reciprocity can be understood as follows. After cooling to room temperature, a particle will have some net moment because domain walls will be distributed to produce incomplete cancellation, in equilibrium with the external field. As the temperature ramps up again, the walls shift within the particle as they seek to minimize the magnetostatic energy. If the particle is cooled back to room temperature, there could be a net magnetization loss, giving rise to the observed low temperature tails. The domain walls may not be destroyed until the temperature is near T_c and some fraction of remanence could persist, giving rise to high temperature tails.

The data of Dunlop and Özdemir (2001) were plotted with the X-axis normalized to the total pTRM acquired and not the initial TRM as is traditional in Arai plots. That resulted in the false impression that the correct answer would be obtained by using the slope of the line connecting the TRM and the total pTRM. The consequence of MD behavior is a strong bias in the resulting paleointensity estimate was later shown by Krása et al. (2003) (Figure 3). They performed KTT-type experiments on carefully sized magnetite specimens ranging from SD particles of 60 nm size to ~12 μm MD particles. The laboratory field in which the TRMs were imparted was 60 μT. Specimen MGH1 (60 nm magnetite, Figure 3a) recovered the original field with excellent accuracy (~59 μT) while the larger grain sizes of W4 (7 μm) and W6 (12 μm) (Figure 3b and c, respectively) are increasingly biased to low values (54 and 42 μT, respectively). These data suggest strongly that MD grains should not be used for paleointensity analysis.

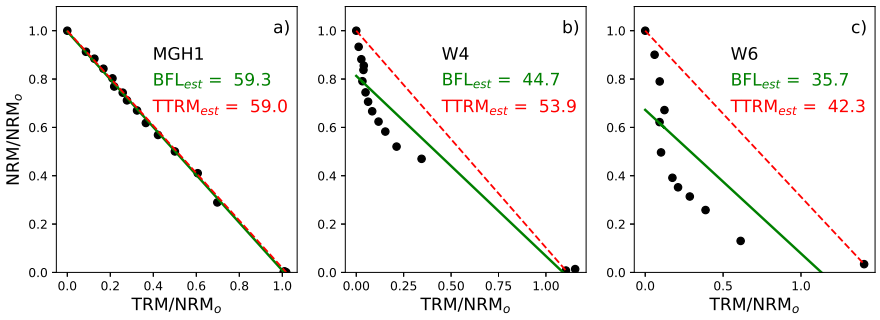

Figure 3. Examples of Arai plots for specimens with known grain sizes from Krasa et al. (2003). Magnetite with sizes: a) 23 nm, b) 7 μm, and c) 12 μm. BFL$_{est}$ is the estimated field from the best-fit heavy green lines and TTRM$_{est}$ is estimated from the total TRM (slopes of dashed red lines).

The sag (downward curvature) in the Arai plots of Krása et al. (2003) results from MD behavior, in which the unblocking temperature spectrum is shifted to lower values relative to the blocking temperature (Figure 1d-f) and the shift is caused by the resulting low temperature pTRM tails (Dunlop & Özdemir, 2001). While the existence of 'tails'

has long been known (Shashkanov & Metallova, 1972), and Dunlop and Özdemir (2001) showed that MD grains have both high and low temperature pTRM tails, it is not clear that domain walls are the only cause of 'sagging' in Arai plots. Smaller non-uniformly magnetized particles without domain walls (vortex state particles) may also be responsible for tails, with unknown consequences for the success of the paleointensity experiment. Unfortunately, flower and vortex state structures (frequently referred to as "pseudo-single domain" grains after Stacey et al. (1961)) are more difficult to understand than either SD particles (which obey Néel theory) or MD particles (which are large enough for domain structures to be imaged easily, e.g. (S. L. Halgedahl, 1993; de Groot et al., 2014)).

1.3 Sagging in natural samples

Many natural samples also have sagging, zig-zagging, hooked, or S-shaped Arai plots. The non-linear behavior is frequently attributed to MD grain sizes. Paterson (2011) developed a statistic to quantify curvature whereby $\vec{k}$ is the inverse of the radius of a best-fit circle. Positive values result from sagging, while negative values result from upward bowed curvature. Paterson (2011) suggested a threshold value of ± 0.164 to detect a significant MD remanence contribution. A version of the $\vec{k}$ statistic, modified to consider only the portion of the Arai plot used in the intensity calculation (k'), has been adopted in paleointensity experiments (Cromwell et al., 2015) to eliminate non-linear Arai plots from paleointensity interpretations. The practical motivation for excluding results with significant curvature comes from empirical comparisons of 'straight' and 'curved' results from specimens that share a common field during cooling, e.g., sister specimens from the same lava flows.

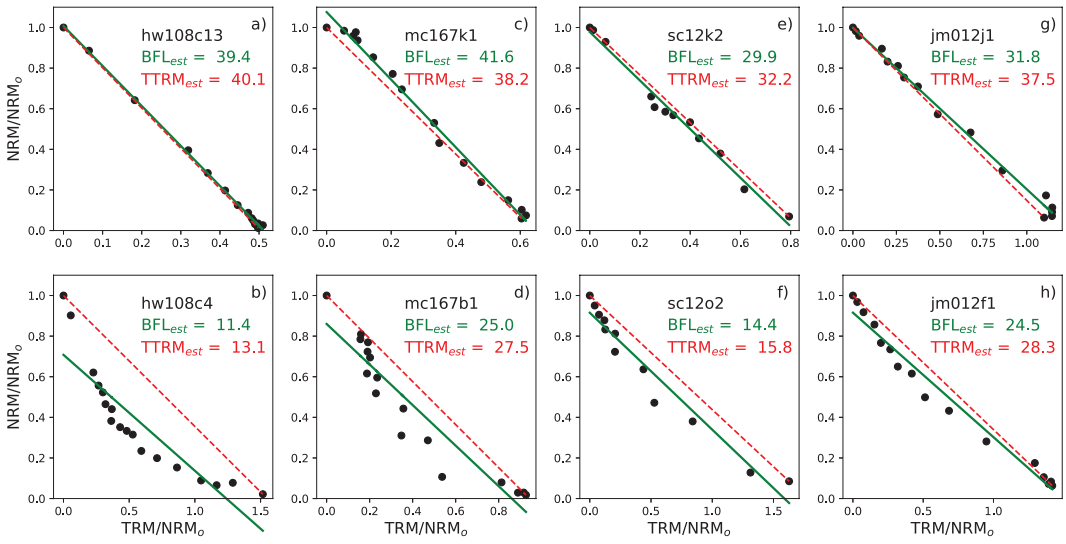

Figure 4. Examples of Arai plots for specimen pairs from the same lava flow with one 'straight' (top panel) and one 'curved' (lower panel). BFL$_{est}$ is the field intensity estimated using the best-fit line (solid green line) and TTRM$_{est}$ is that from the total TRM (dotted red line). a-b) Specimens from the 1859 lava flow on Hawaii from the data set of Cromwell et al. (2015). The IGRF estimate for the field at that time and place is 38.7 μT. c-d) Specimens from site mc167 of Lawrence et al. (2009). e-f) Specimens from site sc12 of Sbarbori et al. (2009). g-h) Specimens from site jm12 of Cromwell et al. (2013). Solid and dashed lines and intensity estimates are as in Figure 3.

Examples of pairs of specimens from the same lava flow are shown in Figure 4 for four published data sets (Cromwell et al., 2015; Lawrence et al., 2009; Sbarbori et al., 2009; Cromwell et al., 2013). In each case the estimated field strength from the specimens with curved Arai plots is lower than for those with straight Arai plots and where the ancient field is known (hw108 of Cromwell et al. (2015)), the specimen with a straight Arai plot gave an accurate answer (within 0.4 μT). Sbarbori et al. (2009) further noted that when specimen sc11e2 with a curved Arai plot (not shown) was given a laboratory TRM and the IZZI experiment was repeated, the Arai plot was straight. Investigating this 'fragile' curvature is the motivation for the present study, the first results of which were published by Shaar and Tauxe (2015). We note that fragile curvature may also be responsible for the 'drawer storage effect' noted by Shaar et al. (2011).

1.4 Aging experiments for natural samples

Shaar and Tauxe (2015) investigated the evolution of Arai plot curvature over time by giving a fresh TRM to a selection of specimens whose Arai plots were curved in the original studies. The fresh laboratory TRM was then subjected to an IZZI paleointensity experiment. As seen previously, the Arai plots were much straighter than those in the original experiments; they displayed what we here call 'fragile curvature'. The specimens were then given another laboratory TRM and 'aged' in the same field for two years. For many specimens, the Arai plot curvature increased and the resulting intensity estimates were biased to low values relative to the laboratory field.

Santos and Tauxe (2019) built on the results of Shaar and Tauxe (2015) by adding a number of specimens whose original Arai plots were not significantly curved (see Table 1 for sampling details). They gave sets of specimens from 'straight' and 'curved' samples a fresh TRM and subjected them to an IZZI paleointensity experiment (Yu et al., 2004; Tauxe & Staudigel, 2004) as in Shaar and Tauxe (2015). Santos and Tauxe (2019) used the k' statistic of Cromwell et al. (2015), which considers only a portion of the experimental data (as opposed to $\vec{k}$ of Paterson (2011)); we re-evaluate the results of Santos and Tauxe (2019) here using the original $\vec{k}$ statistic of Paterson (2011) (see Table 2 for values used in this study).

Locations	Lat.	Long.	Lithology	Age range	Citation DOI
McMurdo (mc)	-76.23	-167.43	basalt	1.26-2.28 Ma	10.1029/2008GC002072
Socorro Island (sc)	18.78	-110.98	trachyte	0.35-0.55 Ma	10.1186/BF03352899
Hawaii (hw)	19.90	-155.58	basalt	1843 CE	10.1016/j.pepi.2014.12.007
Jan Mayen (jm)	71.03	-8.29	basalt	0.2-0.45 Ma	10.1002/ggge.20174
Costa Rica (cr)	9.93	-84.09	basalt	< 2 Ma	10.1002/ggge.20199

Table 1. Locations, lithologies, age ranges, and citations for samples used in the study by Santos and Tauxe (2019) and investigated here. Lat: latitude in °N. Long.: longitude in °E.

The behavior of the specimens in the original IZZI experiments is shown in Figure 5a-d; the 'fresh' TRMs are shown in Figure 5e-h, and curvature values are summarized in Figure 6 and Table 2. We use here a value of $|\vec{k}| \leq 0.164$ as 'straight' (S) and values $|\vec{k}| > 0.164$ as 'curved' (C). A few specimens in the Santos and Tauxe (2019) study yielded results with significantly negative $\vec{k}$ values (bowed upward), which are not the focus of the current investigation and will not be considered further.

Santos and Tauxe (2019) found four categories of behavior based on a comparison of Arai plot curvature in the original versus 'fresh TRM' plots (Figures 5). These are summarized in Figure 6 and Table 2.

1. The SS group (Figure 6) comprises sister specimens whose Arai plots for both the original NRM (Figure 5a) and the 'fresh' laboratory TRM (Figure 5e) were classified as 'straight' (S) by the Paterson statistic.
2. The SC group comprises sister specimens whose Arai plots for the original NRM (Figure 5b) were 'straight', but the 'fresh' laboratory TRM (Figure 5f) was curved (C). This high curvature value results from the high temperature 'hook' which was not well expressed in the original experiments owing to differences in experimental design.
3. The CS group comprises sister specimens whose original Arai plots were 'curved' (Figure 5c) but the fresh TRMs (Figure 5g) were straight.
4. The CC group comprises sister specimens whose original Arai plots were 'curved' (Figure 5d) and for which the fresh TRM was also curved, although in all cases less than the original curvature (Figure 5h).

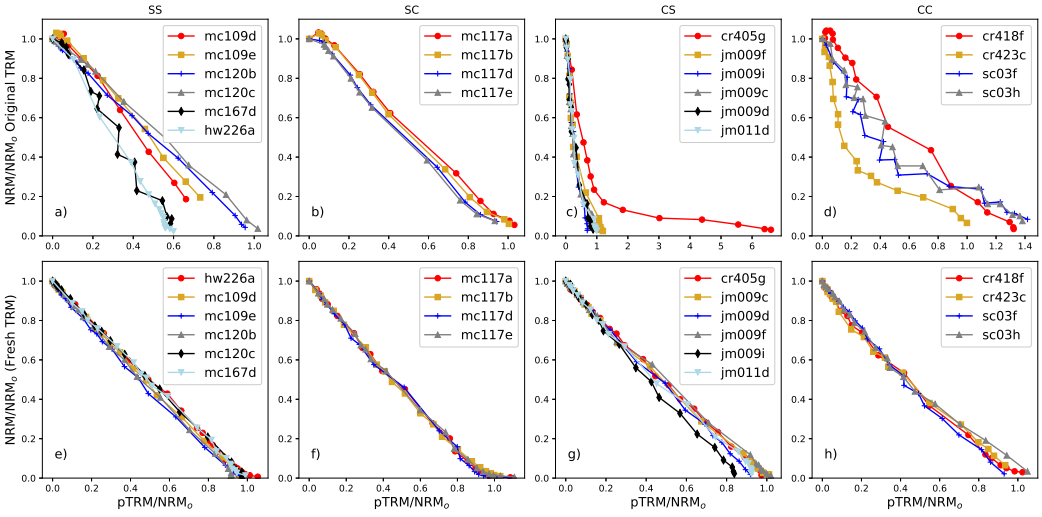

Figure 5. Arai plots for specimens from Santos and Tauxe (2019) and references therein. a, e) SS behavior; b, f) SC behavior; c, g) CS behavior; and d, h) CCbehavior. Top row: Arai plots from the original studies. Bottom row: same as top row, but for the fresh TRM experiments of Santos and Tauxe (2019). Values for curvature are listed in Table 2.

For CS and CC behaviors, all of the 'fresh' TRM results are straighter than in the original experiments, as observed first by Sbarbori et al. (2009), but the CS samples became 'straight' as quantified with the curvature criterion of Paterson (2011) while the CC samples remained somewhat curved. We know from Dunlop and Özdemir (2001) and Krása et al. (2003) (among others) that MD-dominated samples have significant curvature even for freshly imparted TRMs (Figure 3). The curvature in our natural samples (CS and CC) is not reproducible in the fresh TRMs and is not easily explained by MD behavior alone. We call this behavior 'fragile' curvature.

Several questions regarding this 'fragile' curvature spring to mind.

- Does fragile curvature develop over time as suggested by Shaar and Tauxe (2015)?
- Are paleointensity estimates from Arai plots with fragile curvature generally biased (as are results from MD dominated curvature)?
- Does fragile curvature depend on the strength/direction of the aging field?
- What causes fragile curvature?

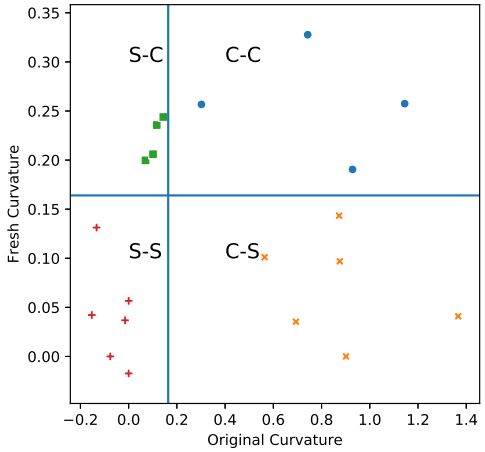

Figure 6. Comparison of curvature as quantified by $\vec{k}$ for the fresh TRMs of Santos and Tauxe (2019) versus original TRMs (see Table 1 for references). Specimens from samples with low curvature (S) either remained straight (SS) or became significantly curved (SC) after being given a fresh TRM. Specimens from samples with high curvature (C) either became straight (CS) or remained curved (CC) after being given a fresh TRM. All CC specimens have significantly less curved Arai plots than in the original experiments, so they have 'fragile' curvature.

To address these issues, we subjected sister specimens from the samples investigated by Santos and Tauxe (2019) (see Table 1) to extensive hysteresis experiments and an 'aging' experiment, similar to that described by Shaar and Tauxe (2015), but with some modifications. We describe in the following sections the experimental details, summarize the results, and consider the questions raised above concerning the temporal stability of fragile curvature and its effects on our ability to estimate ancient field strength.

2 Methods

2.1 Magnetic hysteresis

As part of their rock magnetic characterizations, Santos and Tauxe (2019) measured hysteresis loops for specimens from all samples studied. They plotted so-called 'Day plots' (Day et al., 1977) and estimated the bulk domain stability (BDS) parameter of Paterson et al. (2017). The latter is listed in Table 2 along with the curvature values of the original and laboratory (fresh) TRMs.

First-order reversal curve (FORC) diagrams (Pike et al., 1999) are often used to provide information about domain states, so we subjected specimens from each sample studied by Santos and Tauxe (2019) to the xFORC hysteresis protocol of Zhao et al. (2017) at the Australian National University, Canberra, Australia. Representative conventional FORC diagrams (Pike et al., 1999), and remanence FORC (remFORC), transient FORC (tFORC), and induced FORC (iFORC) diagrams of Zhao et al. (2017) for each of the four categories of interest are shown in Figure 7 with plots generated using the xFORC software available at: https://sites.google.com/site/irregularforc/. We used the 'irregular FORC' measurement protocol of Zhao et al. (2015) and plots were generated with smoothing factors (SF) as noted in the figure caption. The tFORCs are the difference between the conventional FORC (left-hand panel in Figure 7) and the transient-free FORC

Sample	$\vec{k}_{orig}$	$\vec{k}_{fresh}$	TP	BDS	T/R	Lobes	W	FWHM	NPF	APF
mc167d	-0.0000	-0.0173	SS	0.29	0.3427 ± 0.11	NPN+	61	8	5.52	25.6
mc120c	-0.0761	0.0000	SS	0.67	0.0834 ± 0.039	NPN+	46	10	7.53	26.61
mc120b	-0.0149	0.0368	SS	0.64	0.0787 ± 0.04	NPN	65	13	6.53	37.65
mc109e	-0.1330	0.1313	SS	0.43	0.1876 ± 0.08	NPN+	53	5	4.52	17.57
mc109d	-0.1529	0.0422	SS	0.46	0.1534 ± 0.05	NPN+	105	12	5.52	28.61
hw226a	0.0000	0.0566	SS	0.72	0.07 ± 0.05	-	89	24	0.5	46.69
mc117e	0.1438	0.2439	SC	0.40	0.2393 ± 0.09	NPN+	55	1	5.52	20.58
mc117d	0.1164	0.2357	SC	0.36	-	-	-	-	-	-
mc117b	0.1010	0.2060	SC	0.39	0.2533 ± 0.08	NPN+	53	8	4.52	21.59
mc117a	0.0700	0.1997	SC	0.36	0.3659 ± 0.10	NPN+	81	11	7.53	32.63
jm011d	0.8755	0.0969	CS	0.45	0.2636 ± 0.08	NPN+	94	14	8.53	37.65
jm009i	0.5640	0.1011	CS	0.41	0.2435 ± 0.07	NPN+	138	10	9.54	38.65
jm009f	0.9016	-0.0000	CS	0.41	0.2967 ± 0.09	NPN+	184	21	10.54	60.74
jm009d	0.6936	0.0354	CS	0.41	0.2419 ± 0.08	NPN+	141	9	7.53	32.63
jm009c	0.8729	0.1434	CS	0.38	0.395 ± 0.12	NPN+	234	15	11.55	53.71
cr405g	1.3667	0.0409	CS	0.16	0.2268 ± 0.10	NPNPN	125	5	5.52	27.61
sc03h	0.7425	0.3277	CC	0.53	0.1234 ± 0.04	NPNPN	77	5	5.52	31.63
sc03f	0.9284	0.1905	CC	0.44	0.157 ± 0.05	NPN+	61	4	5.52	18.57
cr423c	1.1446	0.2575	CC	0.31	0.2837 ± 0.12	NPNPN	148	21	9.54	34.64
cr418f	0.3018	0.2567	CC	0.27	0.4134 ± 0.13	NPNPN	151	20	6.53	32.63

Table 2. Summary of statistics and parameters for samples used in this study. $\vec{k}_{orig}$: $\vec{k}$ statistic for the original data recalculated from references cited in Table 1. $\vec{k}_{fresh}$: $\vec{k}$ statistic for paleointensity data from fresh TRMs (recalculated from Santos and Tauxe (2019)). TP: Type of curvature for aged versus fresh $\vec{k}$ statistic of Paterson (2011) where 'S' is 'straight' with $\vec{k} \leq 0.164$ and 'C' is ''curved' with $\vec{k}_{fresh} > 0.164$. BDS is the bulk domain stability parameter of Paterson et al. (2017) as reported by Santos and Tauxe (2019). T/R: ratio of the tFORC and remFORC integrated over FORC Zones 1 and 3, respectively. Lobes: number and sign of iFORC lobes where N = negative and P = positive (see Figure 8). Width: width of FORC distribution along the B_i axis (mT). FWHM: full-width half-maximum value (mT). NPF: Nucleation peak field (mT). APF: Annihilation peak field (mT).

(tfFORC, not shown) while the iFORCs are the difference between the tfFORC and the remFORC (panel second from left in Figure 7). The iFORCs in our experiments have several lobes of negative or positive coercivities (labeled N or R in Figure 7d, h, l, p). In many of our samples, the negative lobe in Zone 1 (e.g., Figure 7h, l) has two parts. These are labeled 'N+' in Figure 7 and Table 2.

There are several ways of characterizing and quantifying aspects of FORC diagrams. One, proposed by Carvallo et al. (2006), is to the plot the width of the coercivity spectrum along the B_i axis, against the full-width half-maximum value (FWHM) for a profile through the peak of the coercivity distribution. The width provides a measure of the non-SD content of the specimen, and FWHM provides a measure of the interaction field distribution for SD grains. Width and FWHM values for specimens measured in this investigation are listed in Table 2.

Another way to characterize FORC behavior is to consider the relationship between fields at which vortices nucleate and are annihilated as described by Novosad et al. (2001). The transient nature of vortex structures is what gives rise to so-called 'transient hysteresis' (Fabian, 2003; Yu & Tauxe, 2005). From results for FeNi nanodots (Novosad et

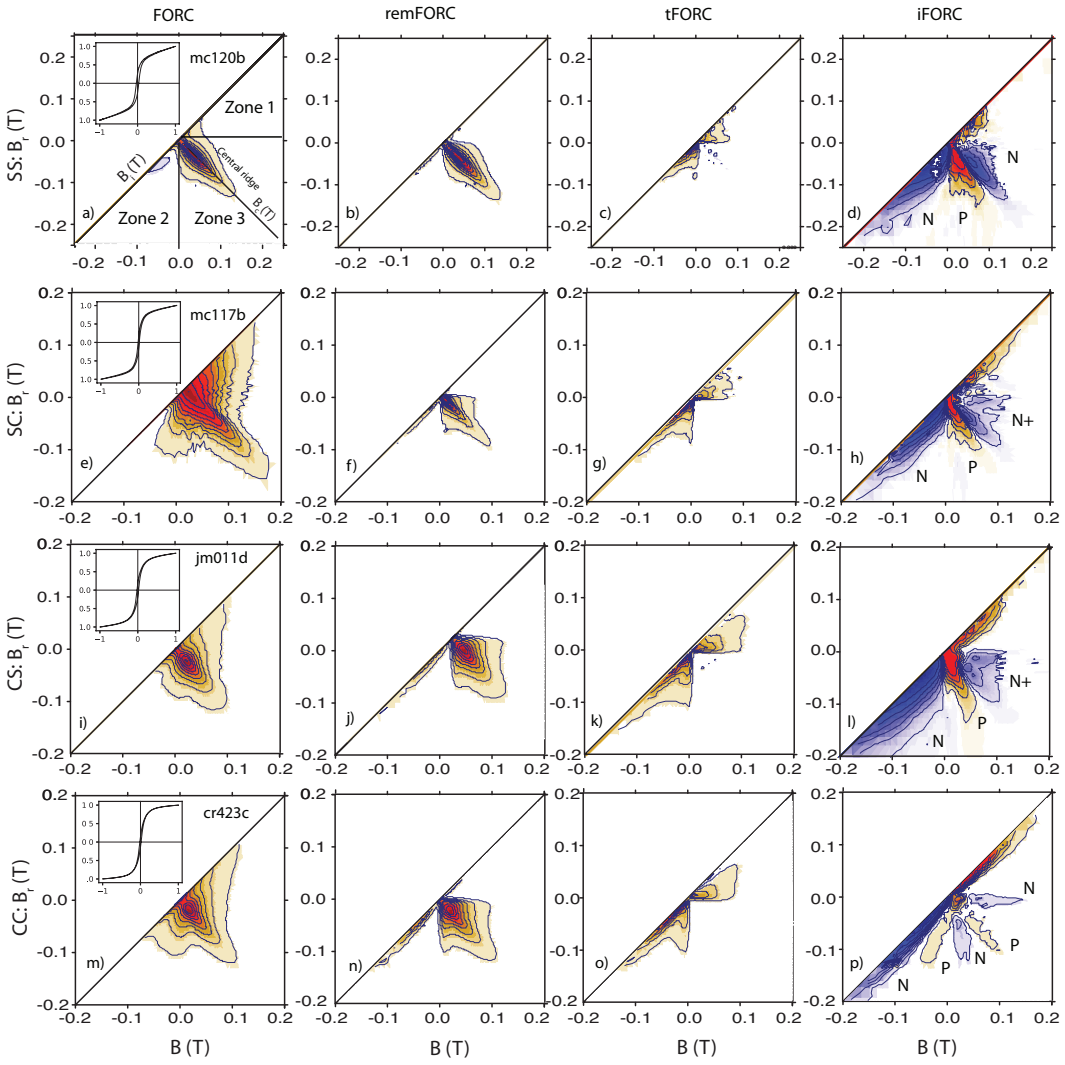

Figure 7. Representative FORC diagrams for samples from the four categories of behavior. Smoothing factor (SF) = 2 for all FORCs, remFORCs, and tFORCs. SF = 3 for all iFORCs except mc120d for which SF = 4. The non-linear color scale factor was 1 for all plots except the iFORCs, which were set to 10. a-d) Specimen from SS sample mc120b. e-h) Specimen from SC sample mc117b. i-l) Specimen from CS sample jm011d. m-p) Specimen from CC sample cr423c. Left-hand panels: conventional first-order reversal curve (FORC) diagrams; insets are the major loops (magnetization (M/M_{max}) versus field (T)). Second panel from left: remanence FORC (remFORC) diagrams. Second panel from right: transient FORC (tFORC) diagrams. Right-hand panels: induced FORC (iFORC) diagrams.

al., 2001), both the nucleation peak field (NPF) and annihilation peak field (APF) depend strongly on grain size with smaller particles having larger nucleation and annihilation fields, and the APF is larger (in the absolute sense) than the NPF because magnetic structures such as a vortex are annihilated in higher fields than they nucleated (Yu & Tauxe, 2005). Estimates of nucleation and annihilation fields from the marginal field distributions in the tFORC diagram are illustrated in Figure 8 and the peak fields observed in our experiments are listed in Table 2.

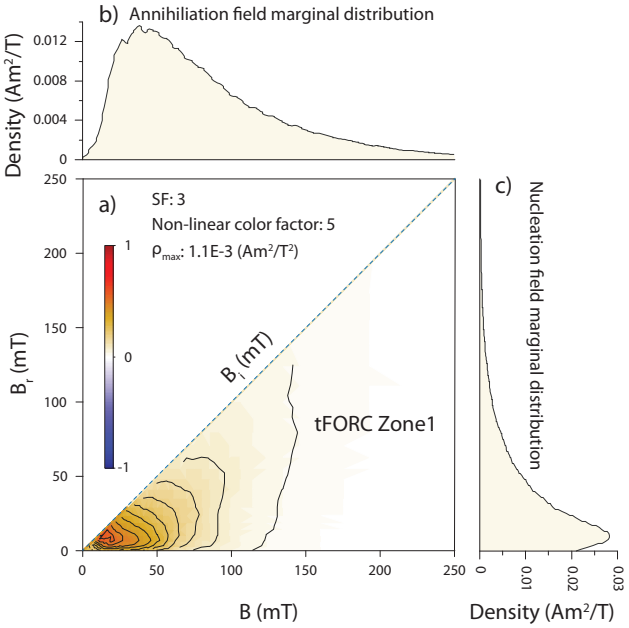

Figure 8. Example of the marginal distribution of nucleation and annihilation fields from Zone 1 of the tFORC distribution. a) Zone 1 of the tFORC distribution for sample jm011d. b) and c) Marginal distributions of the annihilation and nucleation fields, respectively. The smoothing factor (SF) and non-linear color scale for the FORC diagram are specified in the inset.

A third way of quantifying FORC behavior is to calculate the ratio of transient hysteresis to remanence hysteresis by integrating the FORC response over Zone 1 of the tFORC diagram and that of Zone 3 of the remFORC diagram. The latter is dominated by SD grains while the former is dominated by larger grains with transient hysteresis behavior. This ratio (T/R) should reflect the concentration of grains with transient hysteresis behavior (vortex and/or MD magnetic grains) relative to SD grains, which have no transience. We list values of T/R with uncertainties in Table 2.

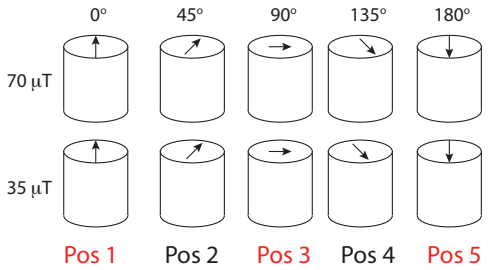

Figure 9. Design of the aging experiment. Sister specimens for each sample from Santos and Tauxe (2019) were given a fresh TRM along the direction of the arrows in a laboratory field of 70 μT. Specimens were placed in one of five positions (Pos 1- Pos 5) in either a 70 μT or 35 μT field.

2.2 Aging and IZZI experiments

Ten sister specimens of the same samples used by Santos and Tauxe (2019) were given a fresh TRM in a laboratory field of 70 μT as in Santos and Tauxe (2019). Instead of subjecting them immediately to the paleointensity experiment, they were allowed to age for two years in laboratory fields of either 35 or 70 μT in five orientations: parallel to the field used to impart the fresh TRM (Pos 1), or at increasingly large angles (Pos 2 - Pos 5) in Figure 9. We consider results from Positions 1, 3, and 5 in this paper; the other positions were reserved for other ongoing experiments. After aging for two years, each specimen from positions 1, 3, and 5 in the two laboratory fields of 35 and 70 μT were subjected to the IZZI experiment.

3 Results

3.1 FORCs

Representative FORC diagrams are shown in Figure 7. We also list the values of various hysteresis parameters considered in this investigation in Table 2.

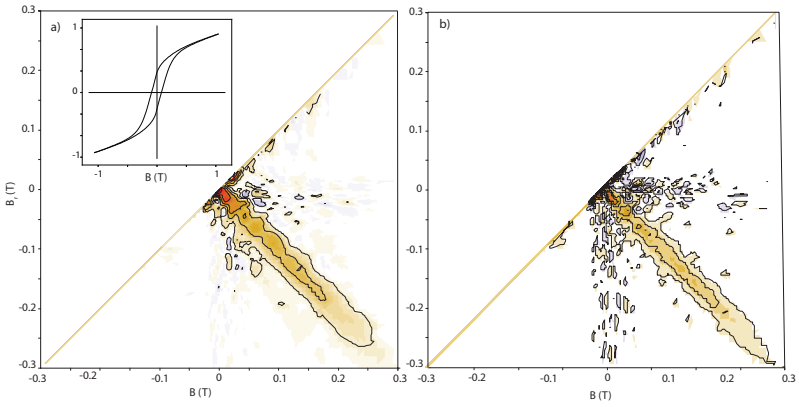

Figure 10. a) Conventional FORC diagram for hw226a. SF = 3; Non-linear color scale factor = 2. b) RemFORC for same specimen as in a). See description in the Figure 7 caption for FORC and remFORC diagrams.

The SS specimen from sample mc120b has dominantly SD behavior (Figure 7a) with a prominent 'central ridge' (Zone 3) and closed FORC contours that are characteristic of non-interacting uniaxial SD populations (Roberts et al., 2000; Egli et al., 2010). Non-interacting SD grains should also have no transient hysteresis (Yu & Tauxe, 2005; Fabian, 2003; Zhao et al., 2017; Harrison et al., 2019), which is consistent with the subdued tFORC signal (Figure 7c). The remFORC diagram (Figure 7b) is similar to the conventional FORC diagram, except that the conventional FORC diagram has a negative lobe along the lower left-hand axis (Zone 2), which is also characteristic of uniaxial SD particles (Muxworthy et al., 2004; Newell, 2005; Egli et al., 2010). The positive lobes in Zone 2 of the remFORC diagrams suggest the presence of viscous grains near the superparamagnetic (SP)/uniaxial SD threshold size (Pike et al., 2001; Zhao et al., 2017). The iFORC diagrams for most SS specimens (Figure 7d) also contain a triplet of lobes (negative-positive-negative or NPN) that are an indication of dominantly uniaxial SD behavior (Zhao et al., 2017; Harrison et al., 2019). We note that one of the SS specimens (hw226a) has no transience in its tFORC diagram (Figure 10; it is the most SD of all the samples.

In contrast to the SS example, the CC specimens (e.g., from sample cr423c; Figure 7m-p) have no negative lobe associated with uniaxial SD particles in Zone 2 of the

FORC diagram (Figure 7m). The conventional FORC diagram for this specimen has a tri-lobate 'pirate hat' shape associated with multi-vortex (MV) behavior (Lascu et al., 2018). The tFORC distribution has distinctive lobes (Figure 7o) and the iFORC diagram (Figure 7p) has five lobes (NPNPN). The lobate tFORC distribution and the NPNPN iFORC lobe structure are thought to be manifestations of vortex state behavior (Zhao et al., 2017). The wide distribution along the B_i axis is also associated with coarse magnetic grain sizes. We list the width as estimated by Carvallo et al. (2006) in Table 2. We interpret the CC series of FORC diagrams as indicative of dominantly coarse grain sizes in the large vortex size range, including single vortex structures and multi-vortex domain states and perhaps also a MD component.

SC specimens (e.g., mc117b in Figure 7e-h) have elements in common with both SS samples (e.g., FORC central ridge; Figure 7e) and CC samples (e.g., tFORC lobes; Figure 7g). The iFORC diagram (Figure 7h) has three lobes (labeled NPN+) compared to the five in the CC samples and the three in some of the SS samples, and the width along the B_i axis is not nearly as large as for the CC sample (see Figure 7m and Table 2). Interestingly, the negative lobe in Zone 1 of the iFORC diagram (Figure 7h) has two "wings". We term these features NPN+ in Table 2. One explanation for the N+ feature is that it represents a combination of large grain sizes, like in the CC specimens (the N lobe in Zone 3) and the N lobe along the central ridge as in the SS specimens. Thus, the FORC behavior of such specimens is consistent with a broad grain size distribution ranging from fine (SP-SD) to coarse (MD-like). Hints of MD behavior are also suggested by negative cooling rate corrections for the sister specimens studied by Santos and Tauxe (2019); as reviewed by Santos and Tauxe (2019) and references therein, negative cooling rates are usually associated with domain walls (i.e., MD grains).

CS specimens (e.g., jm011d in Figure 7i-l) also have elements in common with both the SS and CC samples. The FORC distribution along the B_i axis (Figure 7i) is narrower than for cr423c (Figure 7m, Table 2) and the tFORC diagram (Figure 7k) has 'wings' rather than the lobate structure in Zone 2 that is observed for both the SC and the CC samples, both of which suggest a significant contribution from coarse magnetic grains. In contrast, the iFORC diagram (Figure 7l) has only the three lobes (NPN+) as in the SC specimens. We interpret the FORC results as indicating a broad distribution of SP/SD to large vortex or perhaps even MD grain sizes.

The Carvallo plot (Carvallo et al., 2006) shown in Figure 11a suggests that none of the samples investigated here have FWHM values in excess of the suggested threshold value of 29 mT, which likely rules out strong magnetostatic interactions. However, six samples have width values in excess of the 132 mT threshold value of Carvallo et al. (2006). They suggested that these might be expected to cause failure of paleointensity experiments because of non-SD magnetic behavior. All of the samples that fail the width criterion have either CC or CS behavior and exhibit 'fragile curvature'. The specimen from sample cr405g also has CS behavior and a width (125 mT) close to the threshold value. Interestingly, some of the CC group specimens do not fail this criterion.

A plot of annihilation peak field versus nucleation peak field (Figure 11b) has a single outlier (hw226a), while data from other specimens appear to be related linearly to each other, as expected for vortex nucleation and annihilation. The FORC and remFORC diagrams for hw226a (Figure 10) are different from the other FORC diagrams (e.g., Figure 7) for SS specimens. This specimen has a strong central ridge along the B_c axis that is characteristic of uniaxial SD grains (Egli et al., 2010) and coercivities are much higher than the rest (note scales on the FORC diagrams). The respective remFORC diagram (Figure 10b) is nearly identical (although noisier) to the conventional FORC and there is little transient or induced behavior (not shown). This sample, a quenched flow top from Hawaii, is perhaps the best example of SD dominated behavior among the samples studied here.

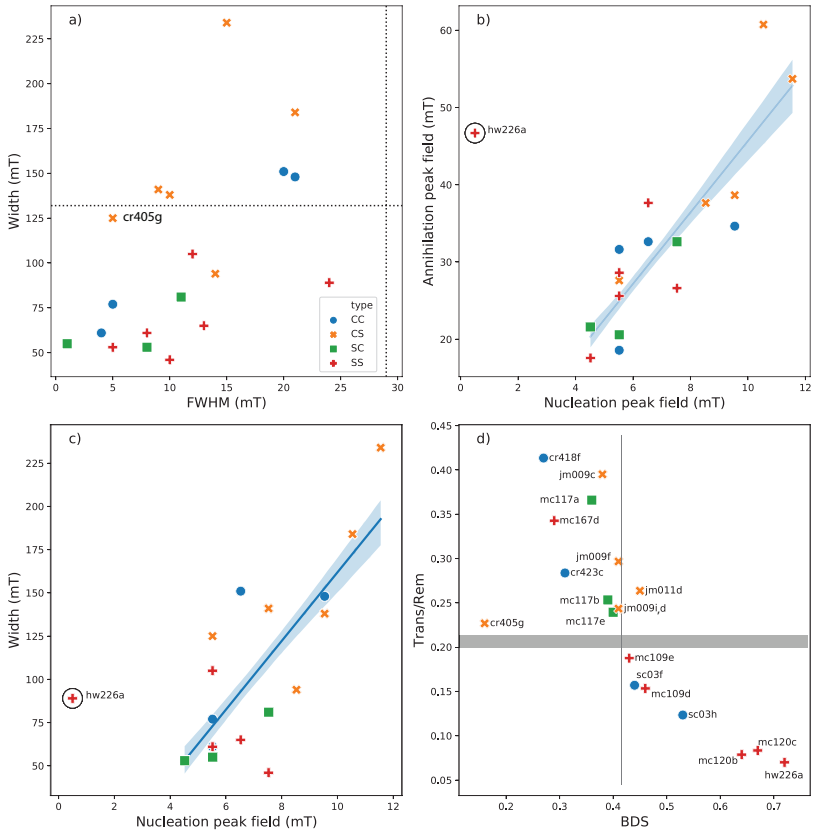

Figure 11. a) 'Carvallo plot' (Carvallo et al., 2006) with width of the FORC distribution along the B_i axis plotted against the full-width half-maximum (FWHM) of a vertical profile through the peak of the coercivity distribution. Threshold values recommended by Carvallo et al. (2006) for FWHM and width are 29 mT and 132 mT, respectively. b) Annihilation peak field (APF) versus nucleation peak field (NPF). c) Width versus nucleation peak field (NPF). Best-fit line with bootstrap uncertainty bounds were calculated without including data for specimen hw226a. d) Transience to Remanence ratio (T/R in Table 2) plotted against bulk domain stability (BDS). All values are listed in Table 2).

There is a quasi-linear relationship between the width parameter (Carvallo et al., 2006) and NPF in Figure 11c, apart from hw226a, which is again an outlier. All samples (apart from hw226a), have behavior characteristic of non-SD behavior with evident transient hysteresis. The fact that the sole truly SD sample (hw226a) has the lowest NPF value among the samples reflects the dearth of vortex state particles in this sample.

Both BDS (Paterson et al., 2017) and the T/R statistic proposed here are meant to characterize domain state. To compare the two, we plot the T/R ratios against BDS values (listed in Table 2) estimated for sister specimens by Santos and Tauxe (2019) in Figure 11d. Apart from cr405g, there appears to be an inverse relationship between the two parameters, with higher BDS values associated with lower transient hysteresis. It also appears that the CS samples are shifted to higher T/R values with similar BDS values than the SC or CC samples. Higher BDS values result from higher saturation remanence to saturation magnetization, with values closer to one thought to represent more SD-like behavior. It makes sense, therefore, that higher BDS values are associated with

lower transient hysteresis. We note that all one has to do to estimate BDS is measure the major hysteresis loop (∼10 minutes), while an xFORC experiment takes hours.

3.2 Aging

Results for all IZZI experiments on aged specimens are shown in Figure S1. All but two of the 36 aged specimens in the SS category have $|\vec{k}| \leq 0.164$ and are 'straight' based on that criterion. The two exceptions are specimens from mc109e (mc109e-SB3) and hw226a (hw226a-SB5), which appear to have altered during the experiment as indicated by a remanence vector that bypasses the origin and grows into the direction of the laboratory field (e.g., Figure 12a). These specimens are not discussed further.

In the SC group, results vary strongly as a function of aging position. For position 5 (aging field anti-parallel to the cooling field), none of the eight specimens became significantly curved after aging but for position 1 in the 70 μT aging field all but specimen mc117d-SA1 became significantly curved. However, for the 35 μT aging field, all but one specimen (mc117e) stayed straight. The different behaviors for the different aging conditions may be influenced strongly by inter-specimen variability within the same samples, which all come from the same lava flow (mc117).

Table 3: Summary of aging experiments. Aged/Fresh/Original: specimen names of the aged/fresh/original specimens (see also Table 2). Type: Arai plot behavior category: SS = originally straight, stayed straight with fresh TRM; SC = originally straight, became curved with fresh TRM; CS = originally curved, became straight with fresh TRM; CC = originally curved, stayed curved with fresh TRM. B_{aged}: strength of the aging field in μT. Pos: position of the sample with respect to aging field (see Figure 9). B_{TTRM}: field strength in μT estimated using the total TRM. $\vec{k}_{aged}$: curvature of the aged Arai plot (see also Figure S1).

Aged	Fresh	Original	Sample	Type	B_{age}	Pos	B_{TTRM}	$\vec{k}_{aged}$
mc167d2-SA5	mc167d2-SZb	mc167d2	mc167d	SS	70	5	68.52	0.0016
mc120c-SA5	mc120c-SZb	mc120c1	mc120c	SS	70	5	68.61	0.0493
mc120b-SA5	mc120b-SZb	mc120b1	mc120b	SS	70	5	78.52	0.0000
mc109e-SA5	mc109e-SZb	mc109e1	mc109e	SS	70	5	67.52	0.1144
mc109d-SA5	mc109d-SZb	mc109d1	mc109d	SS	70	5	66.83	0.0822
hw226a-SA5	hw226a-SZb	hw226a5	hw226a	SS	70	5	64.48	0.1383
mc167d2-SB5	mc167d2-SZb	mc167d2	mc167d	SS	35	5	72.18	0.0029
mc120c-SB5	mc120c-SZb	mc120c1	mc120c	SS	35	5	68.21	0.0527
mc120b-SB5	mc120b-SZb	mc120b1	mc120b	SS	35	5	74.28	-0.0083
mc109e-SB5	mc109e-SZb	mc109e1	mc109e	SS	35	5	68.64	0.1042
mc109d-SB5	mc109d-SZb	mc109d1	mc109d	SS	35	5	66.98	0.1402
hw226a-SB5	hw226a-SZb	hw226a5	hw226a	SS	35	5	70.00	0.2666
mc167d2-SA3	mc167d2-SZb	mc167d2	mc167d	SS	70	3	63.43	0.0856
mc120c-SA3	mc120c-SZb	mc120c1	mc120c	SS	70	3	69.64	0.0427
mc120b-SA3	mc120b-SZb	mc120b1	mc120b	SS	70	3	76.96	0.0040
mc109e-SA3	mc109e-SZb	mc109e1	mc109e	SS	70	3	71.11	0.1026
mc109d-SA3	mc109d-SZb	mc109d1	mc109d	SS	70	3	65.45	0.1312
hw226a-SA3	hw226a-SZb	hw226a5	hw226a	SS	70	3	62.38	0.0709
mc167d2-SB3	mc167d2-SZb	mc167d2	mc167d	SS	35	3	69.64	0.0585
mc120c-SB3	mc120c-SZb	mc120c1	mc120c	SS	35	3	72.24	0.0130
mc120b-SB3	mc120b-SZb	mc120b1	mc120b	SS	35	3	86.71	-0.0560
mc109e-SB3	mc109e-SZb	mc109e1	mc109e	SS	35	3	55.50	0.3934
mc109d-SB3	mc109d-SZb	mc109d1	mc109d	SS	35	3	74.42	0.0668

Continued on next page

hw226a-SB3	hw226a-SZb	hw226a5	hw226a	SS	35	3	64.31	-0.0781
mc167d2-SA1	mc167d2-SZb	mc167d2	mc167d	SS	70	1	67.25	0.1130
mc120c-SA1	mc120c-SZb	mc120c1	mc120c	SS	70	1	70.36	0.0754
mc120b-SA1	mc120b-SZb	mc120b1	mc120b	SS	70	1	75.29	0.0296
mc109e-SA1	mc109e-SZb	mc109e1	mc109e	SS	70	1	65.20	0.1755
mc109d-SA1	mc109d-SZb	mc109d1	mc109d	SS	70	1	71.52	0.0986
hw226a-SA1	hw226a-SZb	hw226a5	hw226a	SS	70	1	67.36	0.1225
mc167d2-SB1	mc167d2-SZb	mc167d2	mc167d	SS	35	1	70.38	0.0489
mc120c-SB1	mc120c-SZb	mc120c1	mc120c	SS	35	1	80.07	0.0000
mc120b-SB1	mc120b-SZb	mc120b1	mc120b	SS	35	1	69.50	0.0563
mc109e-SB1	mc109e-SZb	mc109e1	mc109e	SS	35	1	59.40	0.1783
mc109d-SB1	mc109d-SZb	mc109d1	mc109d	SS	35	1	72.00	0.1275
hw226a-SB1	hw226a-SZb	hw226a5	hw226a	SS	35	1	67.18	-0.0000
mc117e-SA5	mc117e-SZb	mc117e2	mc117e	SC	70	5	71.07	0.0970
mc117d-SA5	mc117d-SZb	mc117d2	mc117d	SC	70	5	70.00	0.0820
mc117b-SA5	mc117b-SZb	mc117b1	mc117b	SC	70	5	73.01	0.1423
mc117a-SA5	mc117a-SZb	mc117a1	mc117a	SC	70	5	65.62	0.1478
mc117e-SB5	mc117e-SZb	mc117e2	mc117e	SC	35	5	67.98	0.1512
mc117d-SB5	mc117d-SZb	mc117d2	mc117d	SC	35	5	66.50	0.1110
mc117b-SB5	mc117b-SZb	mc117b1	mc117b	SC	35	5	67.31	0.0680
mc117a-SB5	mc117a-SZb	mc117a1	mc117a	SC	35	5	75.81	0.0928
mc117e-SA3	mc117e-SZb	mc117e2	mc117e	SC	70	3	69.01	0.1739
mc117d-SA3	mc117d-SZb	mc117d2	mc117d	SC	70	3	61.02	0.2002
mc117b-SA3	mc117b-SZb	mc117b1	mc117b	SC	70	3	77.39	0.1129
mc117a-SA3	mc117a-SZb	mc117a1	mc117a	SC	70	3	63.64	0.1967
mc117e-SB3	mc117e-SZb	mc117e2	mc117e	SC	35	3	72.75	0.1255
mc117d-SB3	mc117d-SZb	mc117d2	mc117d	SC	35	3	72.16	0.0772
mc117b-SB3	mc117b-SZb	mc117b1	mc117b	SC	35	3	71.61	0.0793
mc117a-SB3	mc117a-SZb	mc117a1	mc117a	SC	35	3	64.56	0.2030
mc117e-SA1	mc117e-SZb	mc117e2	mc117e	SC	70	1	67.82	0.1910
mc117d-SA1	mc117d-SZb	mc117d2	mc117d	SC	70	1	78.35	0.1616
mc117b-SA1	mc117b-SZb	mc117b1	mc117b	SC	70	1	69.74	0.2022
mc117a-SA1	mc117a-SZb	mc117a1	mc117a	SC	70	1	65.29	0.2277
mc117e-SB1	mc117e-SZb	mc117e2	mc117e	SC	35	1	68.49	0.2017
mc117d-SB1	mc117d-SZb	mc117d2	mc117d	SC	35	1	68.03	0.1066
mc117b-SB1	mc117b-SZb	mc117b1	mc117b	SC	35	1	69.39	0.1358
mc117a-SB1	mc117a-SZb	mc117a1	mc117a	SC	35	1	73.12	0.1108
jm011d1-CA5	jm011d1-CZb	jm011d1	jm011d	CS	70	5	66.10	0.1637
jm009i2-CA5	jm009i2-CZb	jm009i1	jm009i	CS	70	5	74.67	0.1747
jm009f2-CA5	jm009f2-CZb	jm009f2	jm009f	CS	70	5	67.71	0.1728
jm009d1-CA5	jm009d1-CZb	jm009d1	jm009d	CS	70	5	70.95	-0.0000
jm009c1-CA5	jm009c1-CZb	jm009c1	jm009c	CS	70	5	66.22	0.1728
cr405g1-CA5	cr405g1-CZb	cr405g1	cr405g	CS	70	5	68.02	-0.1559
jm011d1-CB5	jm011d1-CZb	jm011d1	jm011d	CS	35	5	67.84	0.2138
jm009i2-CB5	jm009i2-CZb	jm009i1	jm009i	CS	35	5	67.00	0.1834
jm009f2-CB5	jm009f2-CZb	jm009f2	jm009f	CS	35	5	70.53	0.1829
jm009d1-CB5	jm009d1-CZb	jm009d1	jm009d	CS	35	5	69.05	0.1638
jm009c1-CB5	jm009c1-CZb	jm009c1	jm009c	CS	35	5	69.61	0.1573
cr405g1-CB5	cr405g1-CZb	cr405g1	cr405g	CS	35	5	65.51	-0.0694
jm011d1-CA3	jm011d1-CZb	jm011d1	jm011d	CS	70	3	68.01	0.2050
jm009i2-CA3	jm009i2-CZb	jm009i1	jm009i	CS	70	3	69.09	0.1246
jm009f2-CA3	jm009f2-CZb	jm009f2	jm009f	CS	70	3	71.38	0.1979
jm009d1-CA3	jm009d1-CZb	jm009d1	jm009d	CS	70	3	82.95	0.0938
Aged	Fresh	Original	Sample	Type	B_{age}	Pos	B_{TTRM}	$\vec{k}_{aged}$

Continued on next page

jm009c1-CA3	jm009c1-CZb	jm009c1	jm009c	CS	70	3	67.76	0.1761
cr405g1-CA3	cr405g1-CZb	cr405g1	cr405g	CS	70	3	65.06	-0.0447
jm011d1-CB3	jm011d1-CZb	jm011d1	jm011d	CS	35	3	67.32	0.1651
jm009i2-CB3	jm009i2-CZb	jm009i1	jm009i	CS	35	3	70.97	0.1399
jm009f2-CB3	jm009f2-CZb	jm009f2	jm009f	CS	35	3	71.60	0.1632
jm009d1-CB3	jm009d1-CZb	jm009d1	jm009d	CS	35	3	77.40	0.0959
jm009c1-CB3	jm009c1-CZb	jm009c1	jm009c	CS	35	3	71.00	0.1450
cr405g1-CB3	cr405g1-CZb	cr405g1	cr405g	CS	35	3	64.50	-0.0441
jm011d1-CA1	jm011d1-CZb	jm011d1	jm011d	CS	70	1	69.26	0.2065
jm009i2-CA1	jm009i2-CZb	jm009i1	jm009i	CS	70	1	71.51	0.1236
jm009f2-CA1	jm009f2-CZb	jm009f2	jm009f	CS	70	1	73.77	0.1865
jm009d1-CA1	jm009d1-CZb	jm009d1	jm009d	CS	70	1	71.33	0.1222
jm009c1-CA1	jm009c1-CZb	jm009c1	jm009c	CS	70	1	66.36	0.2210
cr405g1-CA1	cr405g1-CZb	cr405g1	cr405g	CS	70	1	71.49	0.0341
jm011d1-CB1	jm011d1-CZb	jm011d1	jm011d	CS	35	1	71.74	0.1492
jm009i2-CB1	jm009i2-CZb	jm009i1	jm009i	CS	35	1	72.29	0.1249
jm009f2-CB1	jm009f2-CZb	jm009f2	jm009f	CS	35	1	67.36	0.1985
jm009d1-CB1	jm009d1-CZb	jm009d1	jm009d	CS	35	1	72.14	0.1758
jm009c1-CB1	jm009c1-CZb	jm009c1	jm009c	CS	35	1	73.89	0.1406
cr405g1-CB1	cr405g1-CZb	cr405g1	cr405g	CS	35	1	65.54	0.0081
sc03h-CA5	sc03h-CZb	sc03h2	sc03h	CC	70	5	67.20	0.1808
sc03f-CA5	sc03f-CZb	sc03f2	sc03f	CC	70	5	63.63	0.2261
cr423c-CA5	cr423c-CZb	cr423c1	cr423c	CC	70	5	64.91	0.2622
cr418f1-CA5	cr418f-CZb	cr418f1	cr418f	CC	70	5	57.09	0.1394
sc03h-CB5	sc03h-CZb	sc03h2	sc03h	CC	35	5	60.07	0.2495
sc03f-CB5	sc03f-CZb	sc03f2	sc03f	CC	35	5	77.92	0.2381
cr423c-CB5	cr423c-CZb	cr423c1	cr423c	CC	35	5	71.09	0.2404
cr418f1-CB5	cr418f-CZb	cr418f1	cr418f	CC	35	5	72.82	0.3024
sc03h-CA3	sc03h-CZb	sc03h2	sc03h	CC	70	3	73.74	0.1199
sc03f-CA3	sc03f-CZb	sc03f2	sc03f	CC	70	3	62.54	0.1856
cr423c-CA3	cr423c-CZb	cr423c1	cr423c	CC	70	3	80.90	0.4766
cr418f1-CA3	cr418f-CZb	cr418f1	cr418f	CC	70	3	75.46	0.3179
sc03h-CB3	sc03h-CZb	sc03h2	sc03h	CC	35	3	56.38	0.2246
sc03f-CB3	sc03f-CZb	sc03f2	sc03f	CC	35	3	41.04	0.3044
cr423c-CB3	cr423c-CZb	cr423c1	cr423c	CC	35	3	67.00	0.2597
cr418f1-CB3	cr418f-CZb	cr418f1	cr418f	CC	35	3	64.84	0.2868
sc03h-CA1	sc03h-CZb	sc03h2	sc03h	CC	70	1	80.04	0.1469
sc03f-CA1	sc03f-CZb	sc03f2	sc03f	CC	70	1	62.16	0.3762
cr423c-CA1	cr423c-CZb	cr423c1	cr423c	CC	70	1	74.36	0.3021
cr418f1-CA1	cr418f-CZb	cr418f1	cr418f	CC	70	1	68.54	0.2760
sc03h-CB1	sc03h-CZb	sc03h2	sc03h	CC	35	1	70.00	0.1911
sc03f-CB1	sc03f-CZb	sc03f2	sc03f	CC	35	1	53.50	0.4103
cr423c-CB1	cr423c-CZb	cr423c1	cr423c	CC	35	1	67.37	0.2714
cr418f1-CB1	cr418f-CZb	cr418f1	cr418f	CC	35	1	64.62	0.3221
Aged	Fresh	Original	Sample	Type	B_{age}	Pos	B_{TTRM}	$\vec{k}_{aged}$

In the CS group, Arai plots for three of the six specimens aged in the 70 μT field (jm009c, jm009f, and jm011d) became curved in all three positions, while the others remained straight. The Arai plot for a specimen from jm009i also became curved in position 5. Although not significant, the Arai plot for a specimen from cr405g acquired a slight up-bowing in this field, which implies acquisition of a slight but stable viscous remanent magnetization (VRM) (Figure 12b). In the 35 μT aging field in position 1, Arai plots for jm009d and jm009f both became curved. In position 3, only the Arai plot for specimen jm011d became curved. In position 5, all Arai plots except for those for cr405g and jm009c (of the six specimens) became curved.

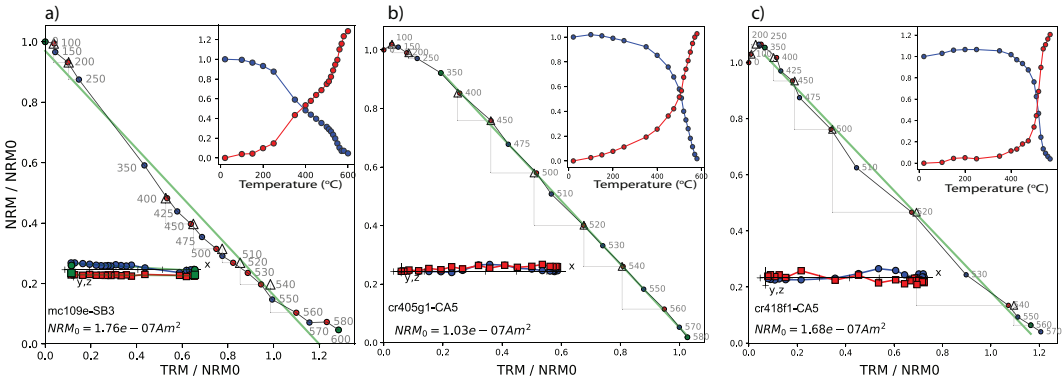

Figure 12. Unusual behavior during the IZZI experiment. Arai plots with best-fit line in green. ZI (IZ) steps are plotted as blue (red) circles; pTRM check steps are plotted as triangles. Lower left insets: Zijderveld (1967) diagrams of remanence decay. X-Y (X-Z) projection plotted as blue circles (red squares). Upper right insets: remanence decay (acquisition) plotted as blue (red) symbols. a) Specimen altered during the experiment. b-c) Specimens acquired a VRM during aging in a 70 μT field anti-parallel to the NRM. The plots were made with thellier_gui.py in the PmagPy software package of Tauxe et al. (2016).

In the CC group, the Arai plot for sc03h was straight in positions 1 and 3 at 70 μT; the Arai plot for cr418f was straight in position 5. This specimen (cr418f-CA5) appears to have acquired a VRM parallel to the magnetizing field (antiparallel to the NRM), which was only removed by about 350°C (Figure 12c). All other Arai plots remained curved.

4 Discussion

4.1 Does fragile curvature grow over time?

We plot the data from Table 3 in Figure 13a. The curvature in Arai plots for aged specimens, except for the SC group, is generally more positive than for fresh specimens. Shaar and Tauxe (2015) stated that curvature increases when specimens are aged in a laboratory field identical to the original cooling field (which is inconsistent with predictions from Néel (1949) theory). Here, we repeated the experiment with different aging field strengths and directions relative to the fresh TRM, with similar results. Therefore, we take these data to demonstrate that fragile curvature in most lava specimens relevant to absolute paleointensity analysis, particularly those not in the SS group which are finer grained, generally increases through time regardless of aging field strength or direction.

4.2 Are paleointensity estimates from fragile curvature biased?

Using intensities estimated from total TRMs, we plot kernel density estimates for fresh and aged specimens in Figure 13c. Estimates from the 'straight' results (both fresh and aged) are unbiased with average values of 71 and 70 μT, respectively. This contrasts with results from fresh and aged curved experiments, which have average values of 65 and 67 μT, respectively. These results support the hypothesis that curved Arai plots tend to yield intensity estimates that are biased low, while straight Arai plots tend to be more accurate. They also validate the use of the curvature criterion proposed by Paterson (2011) as a useful criterion for evaluating paleointensity data. In both data sets, estimates from curved aged specimens are more accurate than from fresh TRMs perhaps because of the

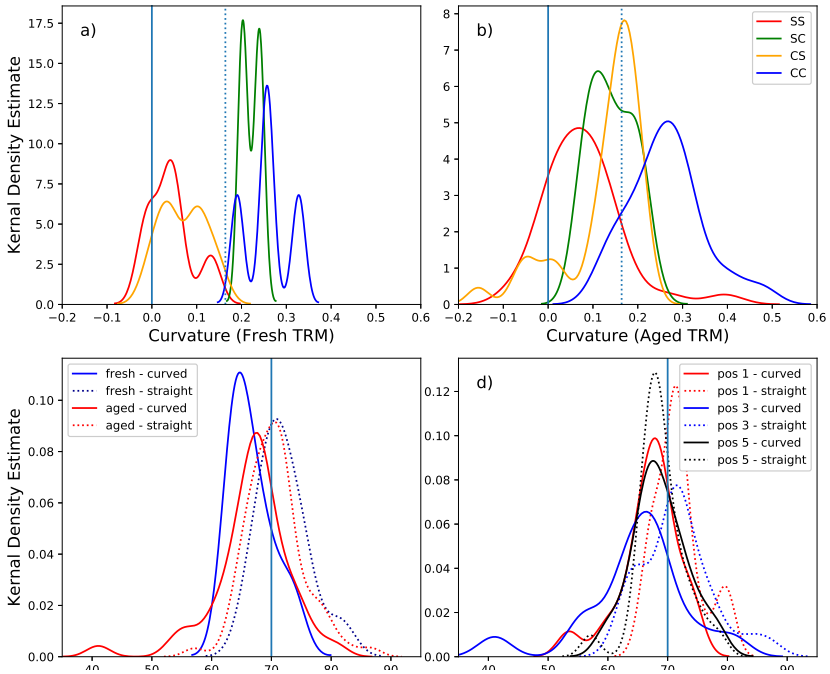

Figure 13. a) Curvature parameter $\vec{k}$ for fresh specimens (data from (Santos & Tauxe, 2019)). The threshold value for $\vec{k}$ of Paterson (2011) is shown as a dotted line. b) Same as a) but for aged specimens. c) Intensity distributions for fresh (blue) specimens versus aged (red) specimens. Dotted (solid) lines are for the curved (straight) specimens. d) Same as c) but as a function of sample position.

increased specimen numbers or a dependence of the paleointensity estimate on direction of the aging field (aging in anti-parallel fields results in less bias for unknown reasons).

To further investigate the role of the angle of the aging field, we plot intensities for the aged groups as a function of aging field orientation in Figure 13d. There is a subtle shift to both wider distributions and lower intensities when aged in an orthogonal field (position 3); thus, both accuracy and precision are affected.

4.3 What causes fragile curvature?

MD grains give rise to curved Arai plots, but the curvature is reproducible in fresh TRMs. What we see here is first a disappearance of curvature in fresh TRMs compared with the original TRMs, followed by growth of curvature over time. Curvature is produced by unequal blocking temperatures relative to unblocking temperatures (see examples in Figure 1). When the unblocking temperature spectrum of the TRM is lower than the blocking temperature spectrum, the result is a downward curvature (sag) of the associated Arai plot and positive $\vec{k}$. Alternatively, when the unblocking temperature spectrum of the TRM is higher than the blocking temperature spectrum, the IZZI experiment does not produce upward curvature of the associated Arai plot; rather, there is a pronounced 'zig-zag', as described by Yu et al. (2004). Downward curvature is produced by low temperature pTRM tails, while the 'hook' observed for the SC group arises from both low and high temperature tails. S-shaped curves, seen in the curves for small MD grains of Dunlop and Özdemir (2001) and in some of the CS and CC specimens results from low temperature pTRM tails with a small contribution from high-temperature pTRM tails. These predictions from phenomenological models such as those shown in Figure 1

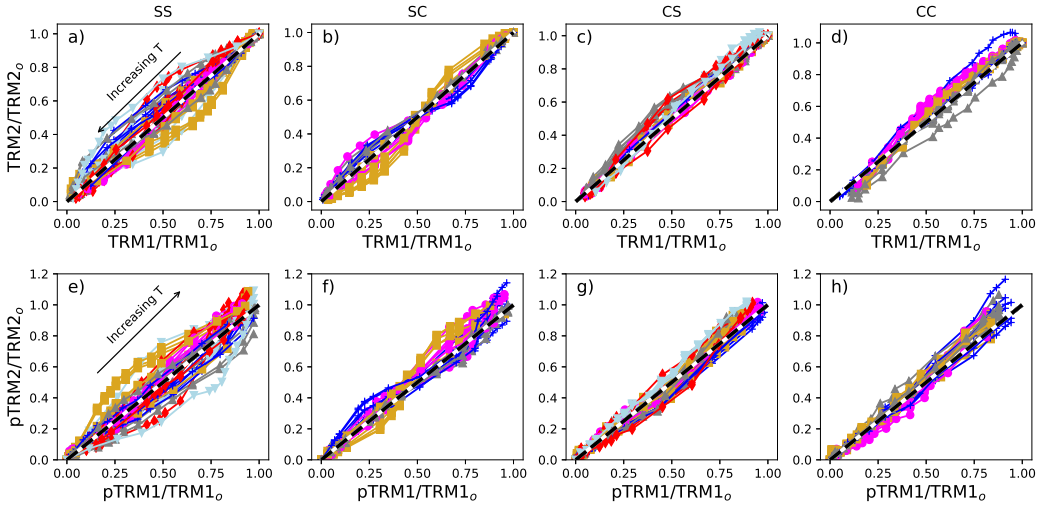

Figure 14. Comparison of (un)blocking temperature spectra between fresh and aged specimens. The curves for demagnetization and remagnetization for the experiments are shown in Figures S2 and S3 in the supplemental information. The expected line of equal (un)blocking at a given step is shown by the black dashed line in each plot. a-d) TRM unblocking (zero field steps). X-axis is magnetization remaining at each temperature step for the fresh TRM (TRM1); Y-axis is magnetization remaining for each aged specimen at the same temperature step (TRM2). The initial TRM is at the upper right-hand corner of the plot. e-h) TRM blocking (infield steps). X-axis is magnetization acquired at each temperature step of the fresh pTRM (pTRM1); Y-axis is magnetization acquired for each aged specimen at the same temperature step (pTRM2). The final pTRM is at the upper right-hand side of the plot. a, e) SS group specimens. b, f) SC group specimens. c, g) CS group specimens. d, h) CC group specimens.

suggest that there should be systematic changes in the blocking and/or unblocking temperature spectra over even two years.

The aging experiment was conducted on 12 sister specimens of each specimen that was subjected to a paleointensity experiment after being given a fresh TRM. Therefore, unlike the experiments of Shaar and Tauxe (2015), no direct comparison of blocking and unblocking temperatures for a given specimen is possible. Nonetheless, we can compare blocking and unblocking spectra in a statistical sense. We show all the demagnetization and remagnetization curves for fresh and aged specimens in Figures S2 and S3 in the Supplemental Information. From those, we plot magnetizations remaining or acquired at each temperature step in the fresh versus aged specimens for each sample in Figure 14.

The top row in Figure 14 is a comparison of the magnetizations remaining in the fresh (x-axis) versus aged (y-axis) specimens during thermal demagnetization. The behavior is controlled by the unblocking temperature spectrum for each specimen. For SS group specimens (Figure 14a), we observe no no systematic trend in demagnetization. For the SC group, there is an 'S' curve with an inflection point at about the median destructive temperature meaning that while the blocking temperatures have shifted in all specimens, some have a pronounced shift at low blocking temperatures while others shifted at high temperatures. In the CS and CC groups, however, all but one specimen appear to have shifted to higher unblocking temperatures (the data points fall above the dashed black line as more magnetization remains at a given step). Therefore, for both the CS

and CC groups, there appears to be a consistent shift to high unblocking temperatures across the entire temperature range after aging.

The bottom row in Figure 14 is similar to the top row, but is a comparison of the magnetizations acquired at each temperature step. Again, for the SS group and surprisingly also for the CS group, there is no consistent aging signal. In contrast, for nearly all specimens in the SC and particularly the CC groups, the points plot above the line for aged specimens compared to the fresh specimens. It appears that the blocking temperatures of these groups have shifted to lower temperatures as more magnetization is blocked at a given temperature step in the aged specimens than in the fresh. We note that the sum of all the pTRMs (the total TRM acquired during the paleointensity experiment) is larger than the original TRM and is what leads to a low bias in intensity estimates, similar to the behavior of the synthetic MD specimens of Krása et al. (2003). The IZZI experiment was designed to detect high temperature tails, not low temperature tails, and it might be worth considering the addition of the so-called 'additivity check' of Krása et al. (2003), see also Paterson et al. (2014).

A shift in (un)blocking temperatures with time, particularly in the less SD-like specimens (SC, CS, CC groups) can be understood by considering the energy barriers that control (un)blocking in magnetic particles. A shift to higher unblocking temperatures means a shift to higher stability and a deeper energy well for the magnetic structures. Uniaxial single domain particles have only two stable states at a given temperature step. At the blocking temperature the energy barrier goes from flat to a single hump (E_{max} in Figure 15a).

We argued that fragile curvature is related to the presence of larger particles based on information gleaned from FORC diagrams. All samples with width parameters that exceeded the threshold values proposed by Carvallo et al. (2006) had original Arai plots that were significantly curved (and subsequently became much straighter when given a fresh TRM in the laboratory). However, data for some of these CC or CS type samples fall below the threshold. Moreover, all SS type samples had either no induced magnetization component (hw226a) or the NPN+ iFORC structure (as opposed to NPNPN structures; see Table 2). Similarly, all but one (sc03f) of the CC samples have a five-fold lobate structure (NPNPN) in iFORC diagrams. All SC samples have NPN+ iFORC structures as did all but one of the CS samples (cr405g) which have a NPNPN structure.

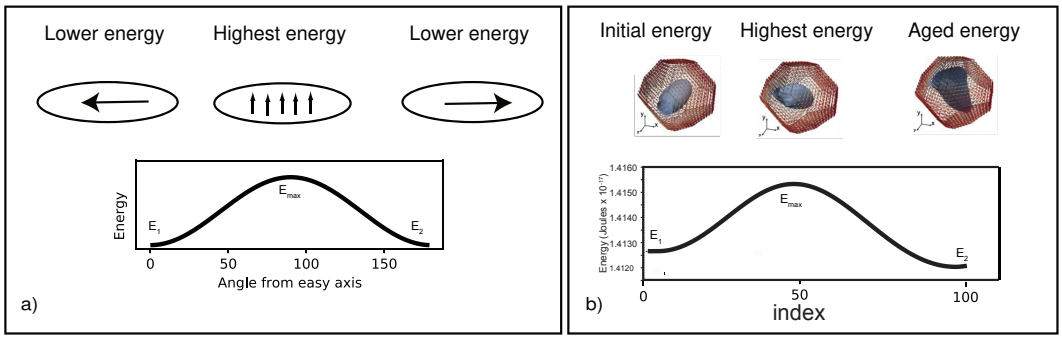

Figure 15. Energy barriers to magnetization switching from one easy axis to the other. a) Néel particle (uniaxial SD). b) Single vortex particle with multiple easy axes.

To understand the magnetic stability of particles larger than single domain, we require the computational approach of micromagnetic modeling (Brown, 1963). Fortunately, much progress has been made with micromagnetic modeling (Williams & Dunlop, 1989; Schabes & Bertram, 1988; Fabian et al., 1996; Tauxe et al., 2002; Nagy et al., 2017; Fabian & Shcherbakov, 2018). Recently, Nagy et al. (2017) suggested, astonishingly, that equidimensional magnetite particles with single vortex (SV) magnetic structures are even more stable paleomagnetically that SD particles. They also discovered a region between the so-called 'flower" and 'vortex' states (Schabes & Bertram, 1988; Williams & Dunlop, 1989), in which the vortex core is aligned with the magnetocrystalline 'hard' direction. In this region, the energy barrier drops precipitously, from relaxation times of longer than the age of the Earth to about a year with a related blocking temperature drop from over 400°C to about 100°C. This may be too low to be involved in the 'aging' process described here, where unblocking temperatures appear to have shifted to higher values all the way up to near the Curie Temperature in Earth-like fields over two years. So, we seek another mechanism that could result in such a shift.

An example of a possible energy landscape for a cuboctohedron in the single vortex size range that switches from one easy axis to another is shown in Figure 15b. In this example, a particle could be blocked in one direction with energy E_1. Thermal energy even at room temperature could be sufficient to exceed $\Delta E = E_{max} - E_1$, allowing the core to switch through the intervening hard direction to the neighboring easy axis with energy $\Delta E = E_{max} - E_2$. The higher energy barrier to return to E_1 could block a magnetic remanence at in a lower energy well and give rise to a higher unblocking temperature. It is, therefore, plausible that fragile curvature results from the relaxation of the magnetic structure from a local energy minimum to a more stable state with higher unblocking temperatures. This process would be analogous to a viscous magnetization, but would result in higher unblocking temperatures than expected for SD particles which are in the range of a few hundred degrees over a period of a few years (Pullaiah et al., 1975).

5 Conclusions

1. There is a distinct difference between the curvature in Arai plots that results from MD behavior (e.g., Dunlop and Özdemir (2001); Krása et al. (2003)) and what we here call 'fragile' curvature, first noticed by Sbarbori et al. (2009) and investigated by Shaar and Tauxe (2015) and Santos and Tauxe (2019). The former is reproducible in the laboratory while the latter disappears when specimens are given a 'fresh' TRM.
2. Curved Arai plots for MD grains yield lower than expected intensity estimates for known laboratory fields (Krása et al., 2003) and results for specimens with 'fragile' curvature are also biased to low values relative to straight Arai plots from the same cooling units.
3. Arai plots for specimens with fragile curvature tend to become more curved when given a fresh TRM and allowed to 'age' in controlled laboratory fields.
4. Experimental protocols and selection criteria that do not test for curvature may yield inaccurate paleointensity results. It is not clear how to 'correct' for this behavior, so it is important to identify it using a curvature criterion.
5. We also find that the failure of the Additivity Law (Thellier & Thellier, 1959) is likely what leads to the low-field bias and that the additivity check criterion (Krása et al., 2003; Paterson et al., 2014) may help detect this problem.
6. A correction for the problem of fragile curvature (and other paleointensity pathologies) may be discovered by simulating paleomagnetic and rock magnetic experiments using micromagnetic models combined with more extensive laboratory 'ground truthing'.

Acknowledgments

This work was supported by NSF grants EAR1547263, NSF-GEO-NERC grant EAR1827263 to LT and WW and by Australian Research Council grant DP190100874 to APR and LT. Data for this project are available at https://earthref.org/MagIC/16963/9b0be19b-e5bc-4cde-8aa4-a8116659542e for the purposes of review and will be made public at https://earthref.org/MagIC/1 upon acceptance of the manuscript. We are grateful for reviews from Grieg Paterson and one anonymous reviewer for improving the manuscript.

References

Abokodair, A. (1977). The accuracy of the Thelliers technique for the determination of paleointensities of the Earth's magnetic field. *PhD Thesis, University of California Santa Cruz*.

Aitken, M., Alcock, P., Bussel, G., & Shaw, C. (1981). Archaeomagnetic determination of the past geomagnetic intensity using ancient ceramics: Allowance for anisotropy. *Archaeometry*, *23*, 53-64.

Biggin, A. (2006). First-order symmetry of weak-field partial thermoremanence in multi-domain (MD) ferromagnetic grains: 2. Implications for Thellier-type palaeointensity determination. *Earth Planet. Sci. Lett.*, *245*, 454-470. doi: 10.1016/j.epsl.2006.02.034

Biggin, A. (2010). Paleointensity database updated and upgraded. *EOS*, *91*, 15.

Brown, W. (1963). *Micromagnetics*. New York: Wiley-Interscience.

Cai, S., Tauxe, L., & Cromwell, G. (2017). Paleointensity from subaerial basaltic glasses from the second Hawaii Scientific Drilling Project (HSDP2) core and implications for possible bias in data from lava flow interiors. *J. Geophys. Res.*, *122*, 8664-8674. doi: 10.1002/2017JB014683

Carvallo, C., Roberts, A., Leonhardt, R., Laj, C., Kissel, C., Perrin, M., & Camps, P. (2006). Increasing the efficiency of paleointensity analyses by selection of samples using first-order reversal curve diagrams. *J. Geophys. Res.*, *111*, B12103. doi: 10.1029/2005JB004126

Coe, R. S. (1967). The determination of paleo-intensities of the earth's magnetic field with emphasis on mechanisms which could cause non-ideal behavior in Thellier's method. *J. Geomag. Geoelectr.*, *19*, 157–178.

Cromwell, G., Tauxe, L., Staudigel, H., Constable, C., Koppers, A., & Pedersen, R.-B. (2013). Evidence for long-term hemispheric asymmetry in the geomagneitc field: Results from high northern latitudes. *Geochem. Geophys. Geosyst.*, *14*. doi: 10.1002/ggge.20174

Cromwell, G., Tauxe, L., Staudigel, H., & Ron, H. (2015). Paleointensity estimates from historic and modern Hawaiian lava flows using basaltic volcanic glass as a primary source material. *Phys. Earth Planet. Int.*, *241*, 44-56. doi: 10.1016/j.pepi.2014.12.007

Cromwell, G., Trusdell, F., Tauxe, L., Staudigel, H., & Ron, H. (2018). Holocene paleointensity of the Island of Hawai'i from glassy volcanics. *Geochem. Geophys. Geosyst.*, *19*, 3224-3245. doi: 10.1002/2017GC006927

Day, R., Fuller, M. D., & Schmidt, V. A. (1977). Hysteresis properties of titanomagnetites: Grain size and composition dependence. *Phys. Earth Planet. Inter.*, *13*, 260–266.

de Groot, L., Fabian, K., Bakellar, I., & Dekkers, M. (2014). Magnetic force microscopy reveals meta-stable magnetic domain states that prevent reliable absolute paleointensity experiments. *Nature Communications*, *5*. doi: 10.1038/ncomms5548

Dodson, M., & McClelland-Brown, E. (1980). Magnetic blocking temperatures of single-domain grains during slow cooling. *J. Geophys. Res.*, *85*, 2625-2637.

Dunlop, D., & Özdemir, O. (2001). Beyond Néel's theories: Thermal demagnetization of narrow-band partial thermoremanent magnetization. *Phys. Earth Planet. Inter.*, *126*, 43-57.

Egli, R., Chen, A., & Winklhofer, M. (2010). Detection of noninteracting single domain particles using first-order reversal curve diagrams. *Geochem. Geophys. Geosyst.*, *11*, Q01Z11. doi: 10.1029/2009GC002916

Fabian, K. (2001). A theoretical treatment of paleointensity determination experiments on rocks containing pseudo-single or multi domain magnetic particles. *Earth Planet. Sci. Lett.*, *188*, 45-48.

Fabian, K. (2003). Some additional parameters to estimate domain state from isothermal magnetization measurements. *Earth Planet. Sci. Lett.*, *213*(3-4),

337-345. doi: 10.1016/S0012-821X(03)00329-7

Fabian, K., Andreas, K., Williams, W., Heider, F., Leibl, T., & Huber, A. (1996). Three-dimensional micromagnetic calculations for magnetite using FFT. *Geophys. J. Int.*, *124*, 89-104.

Fabian, K., & Shcherbakov, V. (2018). Energy barriers in three-dimensional micromagnetic models and the physics of thermoviscous magnetization. *Geophys. J. Int.*, *215*, 314-324. doi: 10.1093/gji/ggy285

Halgedahl, S., Day, R., & Fuller, M. (1980). The effect of cooling rate on the intensity of weak-field TRM in single-domain magnetite. *J. Geophys. Res*, *85*, 3690-3698.

Halgedahl, S. L. (1993). Experiments to investigate the origin of anomalously elevated unblocking temperatures. *J. Geophys. Res.*, *98*, 22443–22460.

Harrison, R., Zhao, X., Hu, P., Sato, T., Heslop, D., Muxworthy, A., ... Roberts, A. (2019). Simulation of remanent, transient, and induced FORC diagrams for interacting particles with uniaxial, cubic, and hexagonal anisotropy. *J. Geophys. Res*, *124*, 12404-12429. doi: 10.1029/2019jb018050

Koenigsberger, J. (1938). Natural residual magnetism of eruptive rocks, Pt I, Pt II. *Terr. Magn. Atmos. Electr.*, *43*, 119-127; 299-320.

Königsberger, J. (1936). Die abhaengigkeit der natuerlichen remanenten magnetisierung bei eruptivgesteinen von deren alter und zusammensetzung. *Beitr. Angew. Geophys.*, *5*, 193-246.

Krása, D., Heunemann, C., Leonhardt, R., & Petersen, N. (2003). Experimental procedure to detect multidomain remanence during Thellier-Thellier experiments. *Phys. Chem. Earth*, *28*, 681-687. doi: 10.1016/S1474-7065(03)00122-0

Lascu, I., Einsle, J., Ball, M., & Harrison, R. (2018). The vortex state in geologic materials: A micromagnetic perspective. *J. Geophys. Res.*, *123*, 7285-7304. doi: 10.1029/2018JB015909

Lawrence, K. P., Tauxe, L., Staudigel, H., Constable, C., Koppers, A., McIntosh, W. C., & Johnson, C. L. (2009). Paleomagnetic field properties near the southern hemisphere tangent cylinder. *Geochem. Geophys. Geosyst.*, *10*, Q01005. doi: doi:10.1029/2008GC002072

Muxworthy, A., Heslop, D., & Williams, W. (2004). Influence of magnetostatic interactions on first-order-reversal-curve (FORC) diagrams: A micromagnetic approach. *Geophys. J. Int.*, *158*, 888-897. doi: 10.1111/j.1365-246X.2004.02358.x

Nagy, L., Williams, W., Muxworthy, A., Fabian, K., Almeida, T., Conbhui, P., & Shcherbakov, V. (2017). Stability of equidimensional pseudo-single domain magnetite over billion year timescales. *Proc. Natl. Acad. Sci. U.S.A.*, *114*, 10356-10360. doi: 10.1073/pnas.1708344114

Néel, L. (1949). Théorie du trainage magnétique des ferromagneétiques en grains fines avec applications aux terres cuites. *Ann. Geophys.*, *5*, 99–136.

Néel, L. (1955). Some theoretical aspects of rock-magnetism. *Adv. Phys*, *4*, 191-243. doi: 10.1080/00018735500101204

Newell, A. (2005). A high-precision model of first-order reversal curve (FORC) functions for single-domain ferromagnets with uniaxial anisotropy. *Geochem. Geophys. Geosyst.*, *6*, Q05010. doi: 10.1029/2004GC000877

Novosad, V., Guslienko, H., Shima, Y., Otani, K., Fukamichi, K., Kitakami, N., & Shimada, Y. (2001). Nucleation and annihilation of magnetic vortices in sub-micron permalloy dots. *IEEE Trans. Magn.*, *37*, 2088-2090. doi: 10.1109/20.951062

Paterson, G. (2011). A simple test for the presence of multidomain behavior during paleointensity experiments. *J. Geophys. Res.*, *116*(B10). doi: 10.1029/2011JB008369

Paterson, G., Biggin, A., Hodgson, E., & Hill, M. (2015). Thellier-type paleointensity data from multidomain specimens. *Phys. Earth Planet. Inter.*, *245*, 117-

133. doi: 10.1016/j.pepi.2015.06.003

Paterson, G., Muxworthy, A., Yamamoto, Y., & Pan, Y. (2017). Bulk magnetic domain stability controls paleointensity fidelity. *Proc. Natl. Acad. Sci. U.S.A.*, *114*, 13120-13125. doi: 10.1073/pnas.1714047114

Paterson, G., Tauxe, L., Biggin, A., Shaar, R., & Jonestrask, L. (2014). On improving the selection of thellier-type paleointensity data. *Geochem. Geophys. Geosyst.*, *15*(4). doi: 10.1002/2013GC005135

Pike, C., Roberts, A., Dekkers, M., & Verosub, K. (2001). An investigation of multidomain hysteresis mechanisms using forc diagrams. *Physics of The Earth and Planetary Interiors*, *126*(1-2), 11-25.

Pike, C., Roberts, A., & Verosub, K. (1999). Characterizing interactions in fine magnetic particle systems using first order reversal curves. *J. Appl. Phys.*, *85*, 6660-6667.

Pullaiah, G., Irving, E., Buchan, K., & Dunlop, D. (1975). Magnetization changes caused by burial and uplift. *Earth Planet. Sci. Lett.*, *28*, 133-143.

Roberts, A., Pike, C., & Verosub, K. (2000). First-order reversal curve diagrams: A new tool for characterizing the magnetic properties of natural samples. *J. Geophy. Res.*, *105*, 28461-28475. doi: 10.1029/2000JB900326

Santos, C., & Tauxe, L. (2019). Investigating the accuracy, precision, and cooling rate dependence of laboratory acquired thermal remanences during paleointensity experiments. *Geochem. Geophys. Geosyst.*, *20*, 383-397. doi: 10.1029/2018GC007946

Sbarbori, E., Tauxe, L., Goguitchaichvili, A., Urrutia-Fucugauchi, J., & Bohrson, W. (2009). Paleomagnetic behavior of volcanic rocks from Isla Socorro, Mexico. *Earth, Planets Space*, *61*, 191-204. doi: 10.1186/BF03352899

Schabes, M. E., & Bertram, H. N. (1988). Magnetization processes in ferromagnetic cubes. *J. Appl. Phys.*, *64*, 1347–1357.

Selkin, P., Gee, J. S., & Tauxe, L. (2007). Nonlinear thermoremanence acquisition and implications for paleointensity data. *Earth Planet. Sci. Lett.*, *256*, 81-89.

Shaar, R., Ron, H., Tauxe, L., Kessel, R., & Agnon, A. (2011). Paleomagnetic field intensity derived from non-SD: Testing the Thellier IZZI technique on MD slag and a new bootstrap procedure technique on MD slag and a new bootstrap procedure. *Earth Planet Sci. Lett.*, *310*(213-224).

Shaar, R., & Tauxe, L. (2015). Instability of thermoremanence and the problem of estimating the ancient geomagnetic field strength from non-single-domain recorders. *Proc. Natl. Acad. Sci. U.S.A.*, *112*, 11187-11192. doi: 10.1073/pnas.1507986112

Shashkanov, V., & Metallova, V. (1972). Violation of Thellier's law for partial thermoremanent magnetizations. *Izv. Earth Physics*, *3*, 80-86.

Smirnov, A., Kulakov, E., Foucher, M., & Bristol, K. (2017). Intrinsic paleointensity bias and the long-term history of the geodynamo. *Sci. Adv.*, *3*. doi: 10.1126/sciadv.1602306

Stacey, F. D., Lovering, J. F., & Parry, L. G. (1961). Thermomagnetic properties, natural magnetic moments, and magnetic anisotropies of some chondritic meteorites. *J. Geophys. Res.*, *66*, 1523-1534.

Tanaka, H., & Kono, M. (1991). Preliminary results and reliability of palaeointensity studies on historical and C^{14} dated Hawaiian lavas. *J. Geomagn. Geoelectr.*, *43*, 375-388.

Tauxe, L., Banerjee, S. K., Butler, R., & van der Voo, R. (2010). *Essentials of Paleomagnetism*. Berkeley: University of California Press.

Tauxe, L., Bertram, H., & Seberino, C. (2002). Physical interpretation of hysteresis loops: Micromagnetic modelling of fine particle magnetite. *Geochem. Geophys. Geosyst.*, *3*, doi:10.1029/2001GC000280.

Tauxe, L., Shaar, R., Jonestrask, L., Swanson-Hysell, N., Minnett, R., Koppers, A. A. P., ... Fairchild, L. (2016). PmagPy: Software package for

765 paleomagnetic data analysis and a bridge to the Magnetics Information
766 Consortium (MagIC) database. *Geochem. Geophys. Geosyst.*, *17*. doi:
767 10.1002/2016GC006307
768 Tauxe, L., & Staudigel, H. (2004). Strength of the geomagnetic field in the
769 Cretaceous Normal Superchron: New data from submarine basaltic glass
770 of the Troodos Ophiolite. *Geochem. Geophys. Geosyst.*, *5*(2), Q02H06,
771 doi:10.1029/2003GC000635.
772 Tauxe, L., & Yamazaki, T. (2015). Paleointensities. In M. Kono (Ed.), *Geomag-*
773 *netism* (2nd Edition ed., Vol. 5, p. 461-509). Elsevier.
774 Thellier, E. (1938). Sur l'aimantation des terres cuites et ses applications
775 géophysique. *Ann. Inst. Phys. Globe Univ. Paris*, *16*, 157-302.
776 Thellier, E., & Thellier, O. (1959). Sur l'intensité du champ magnétique terrestre
777 dans le passé historique et géologique. *Ann. Geophys.*, *15*, 285–378.
778 Williams, W., & Dunlop, D. J. (1989). Three-dimensional micromagnetic modelling
779 of ferromagnetic domain structure. *Nature*, *337*, 634–637.
780 Yu, Y., & Tauxe, L. (2005). On the use of magnetic transient hysteresis in paleo-
781 magnetism for granulometry. *Geochem. Geophys. Geosyst.*, *6*, Q01H14. doi: 10
782 .1029/2004GC000839
783 Yu, Y., Tauxe, L., & Genevey, A. (2004). Toward an optimal geomagnetic field in-
784 tensity determination technique. *Geochem. Geophys. Geosyst.*, *5*(2), Q02H07,
785 doi:10.1029/2003GC000630.
786 Zhao, X., Heslop, D., & Roberts, A. (2015). A protocol for variable-resolution
787 first-order reversal curve measurements. *Geochem. Geophys. Geosyst.*, *16*,
788 1364-1377. doi: 10.1002/2014GC005680
789 Zhao, X., Roberts, A., Heslop, D., Paterson, G., Li, Y., & Li, J. (2017). Magnetic
790 domain state diagnosis using hysteresis reversal curves. *J. Geophys. Res.*, *122*,
791 4767-4789. doi: 10.1002/2016JB013683
792 Zijderveld, J. D. A. (1967). A.C. demagnetization of rocks: Analysis of results. In
793 (p. 254-286). Chapman and Hall. doi: 10.1016/b978-1-4832-2894-5.50049-5